

Effect of hydrogen on the local chemical bonding states and structure of amorphous alumina by atomistic and electrostatic modeling of Auger parameter shifts

Simon Gramatte^{1,2,3,4}, Olivier Politano², Claudia Cancellieri³, Ivo Utke⁵, Lars P.H. Jeurgens³, and Vladyslav Turlo^{1,4,*}

¹Laboratory for Advanced Materials Processing, Empa - Swiss Federal Laboratories for Materials Science and Technology, Feuerwerkerstrasse 39, 3602 Thun, Switzerland

²Laboratoire Interdisciplinaire Carnot de Bourgogne, UMR 6303 CNRS-Université de Bourgogne, 9 Avenue A. Savary, 21078 Dijon Cedex, France

³Laboratory for Joining Technologies and Corrosion, Empa - Swiss Federal Laboratories for Materials Science and Technology, Ueberlandstrasse 129, 8600 Duebendorf, Switzerland

⁴National Centre for Computational Design and Discovery of Novel Materials MARVEL, Empa, Thun, Switzerland

⁵Laboratory for Mechanics of Materials and Nanostructures, Empa - Swiss Federal Laboratories for Materials Science and Technology, Feuerwerkerstrasse 39, 3602 Thun, Switzerland

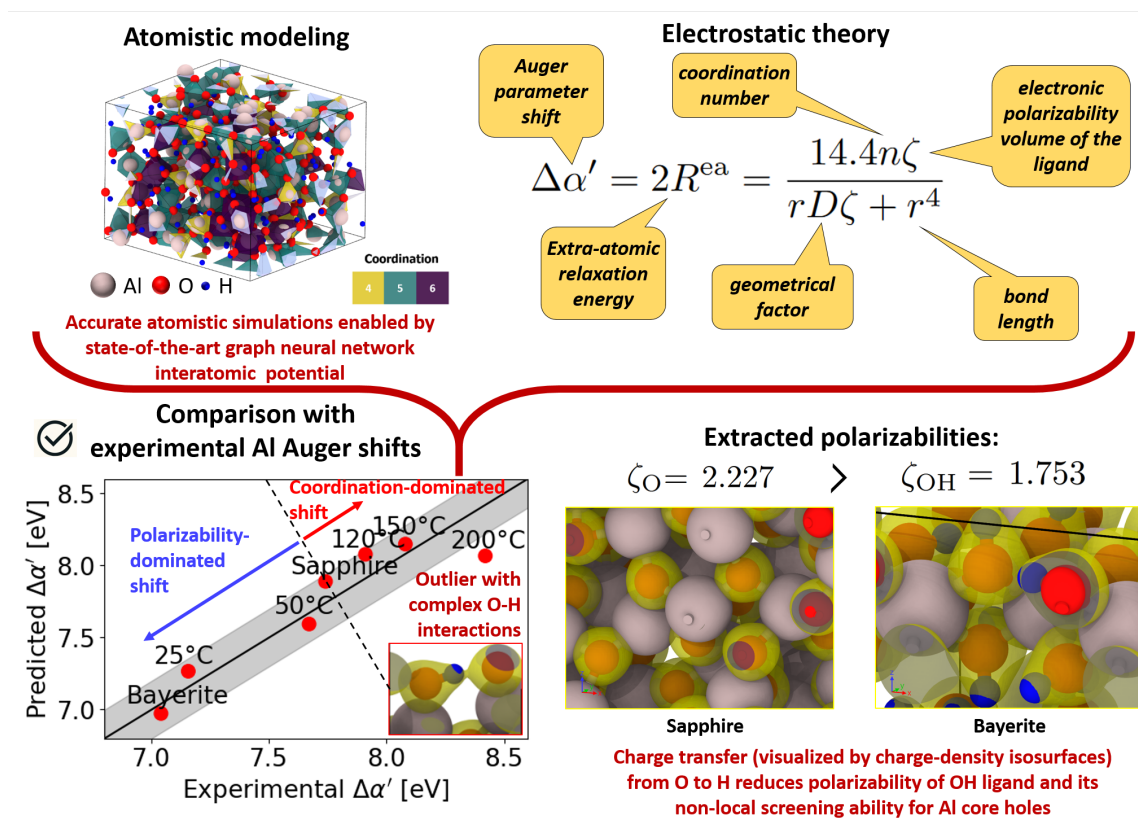
*Corresponding author: Vladyslav Turlo, vladyslav.turlo@empa.ch

August 16, 2024

Abstract

This study discloses the effect of hydrogen impurities on the local chemical bonding states and structure of amorphous alumina films by predicting measured Auger parameter shifts using a combination of atomistic and electrostatic modeling. Different amorphous alumina polymorphs with variable H-content and density, as grown by atomic layer deposition, were successfully modeled using a universal machine learning interatomic potential. The annealing of highly defective crystalline hydroxide structures with experimental H-contents at the corresponding atomic layer deposition temperatures led to excellent agreement between theory and experiment in the density and structure of the resulting amorphous alumina polymorphs. The measured Auger parameter shifts of Al cations in such polymorphs were accurately predicted with respect to the H content by assuming that all H atoms are present in the form of hydroxyl ligands in the randomly interconnected 4-fold, 5-fold, and 6-fold nearest-neighbor coordination spheres of Al. As revealed by a combination of atomistic and electrostatic modeling, the measured Auger shifts with an increase in the H content and an accompanying decrease in the oxide density depend on the complex correlations between local coordination, bond lengths, bond angles, and ligand type(s) around the core-ionized atoms. Moreover, cryogenic X-ray photoelectron spectroscopy is suggested to offer new insights into the local chemical and structural building blocks of crystalline and amorphous oxides by reducing thermal noise. These findings and fundamental knowledge contribute to advancing the design of e.g. hydrogen oxide barrier films, oxide membranes for H separation, H storage materials, and fuel cells for a hydrogen-based economy.

Graphical Abstract



Keywords— molecular dynamics (MD), density functional theory (DFT), electrostatic modeling, hydrogen, amorphous oxide, X-ray photoelectron spectroscopy (XPS), Auger parameter, atomic layer deposition (ALD)

1. Introduction

The energy transition of our society requires an improved fundamental understanding of the chemical interaction of H with different oxide materials [1]. For example, the incorporation and diffusion of atomic H in oxide membranes for H-purification, in oxides for photocatalytic water splitting, as well as in passivated oxides on steel, may affect the mechanical, chemical, and electronic properties and thereby the materials' performance, reliability, and sustainability. In particular, the effect of H impurities on the barrier properties of oxide layers grown by Atomic Layer Deposition (ALD) is of great scientific and technological interest, since hydrogen permeation barriers fabricated by ALD are broadly applied to address specific challenges for transport, handling, and storage of H [2, 1]. ALD also helps in the design of new advanced materials for energy conversion and storage [3, 4, 5, 6, 7, 8, 9], electronics [10, 11], catalysis [12, 13], gas sensing [14], biosensing [15], water purification and gas separation [16, 17], as well as corrosion protection [18, 19].

ALD represents a conventional method for creating functional thin films with remarkable atomic-level precision in thickness [20], ensuring uniform, flawless coverage over complex substrate shapes, including those with high aspect ratios [21] and porous structures [22, 23]. Functioning as a specialized form of chemical vapor deposition, ALD operates through sequential exposure of substrates to vapor-phase precursors, which engage in self-limiting chemical reactions (known as chemisorption) on the substrate's surface [24], thus enabling the precise deposition of different material classes, such as metals [25, 26], simple binary oxides [27, 28, 29], complex multicomponent compounds [30, 31], and 2D materials [32]. The ALD deposition process of barrier films of amorphous alumina (further designated as *am*-Al₂O₃) includes alternating exposure of the activated surface to trimethylaluminum and water having methane as a reaction product. It has been shown that a significant amount of hydrogen can be incorporated into these *am*-Al₂O₃ ALD barrier films, especially at low growth temperatures [33, 34]. These H impurities have a detrimental impact on the mechanical properties [35, 36] while also lowering the dielectric strength [37] and room-temperature thermal conductivity [38] of the *am*-Al₂O₃ films. The density and composition of the *am*-Al₂O₃ ALD films in dependence on their hydrogen content (which is a function of the ALD growth temperature) has been resolved experimentally [33, 34]. However, to fundamentally rationalize the deterioration of the *am*-Al₂O₃ film properties by H incorporation, it is critical to resolve the local chemical bonding state of hydrogen in the amorphous structure, which presents a huge challenge for modern experimental characterization tools.

Tiny changes in the local chemical states and short-range order of *amorphous* oxides, as induced by light element impurities (like hydrogen) and/or upon crystallization, are only accessible by a few chemical-specific analytical techniques, such as X-ray Photoelectron Spectroscopy (XPS) [39, 40, 34], X-ray Adsorption Near-edge and Extended Fine Structure Spectroscopy (XANES/EXAFS) [41] and solid-state Nuclear Magnetic Resonance (NMR) [42]. Unfortunately, NMR analysis is generally not applicable for thin films with thicknesses of a few tenths of nanometers. Carefully chosen and suitable (crystalline) reference materials are key for successful analysis and interpretation of recorded XANES/EXAFS spectra, but often fail to resolve specific nearest-neighbour coordination spheres (NNCS) in the amorphous phase which are not represented by any of its crystalline reference phases (e.g. 5-fold or distorted 6-fold coordination spheres in *am*-Al₂O₃ [43]). Conventional XPS is a very powerful tool for probing local chemical states in oxides up to a probing depth of about 6 nm (using soft Al-K α or Mg-K α radiation) [44]. Recent developments in instrumentation, microelectronics, and detector technologies have enabled routine analysis by hard X-ray photoemission (HAXPES) at synchrotrons worldwide, as well as in the laboratory (using a combination of Al-K α , Ag-K α , Cr-K α and/or Ga-K α X-ray sources) [45]. The increase in kinetic energy of emitted photoelectrons with increasing photon energy is accompanied by an increase in photoelectron probing depth, which enables sampling of the (averaged) local chemical states of the constituent ions in oxides up to depths in the range of 20–30 nm [46]. Moreover, photoemission of deep core-level electrons (e.g. from the 1s shell) by hard X-rays can trigger sharp and intense core–core–core Auger transitions, particularly KL₂₃L₂₃ Auger transitions (see Fig. 1(a)), which can be exploited for local chemical state analysis based on the (modified) Auger parameter (AP), as originally proposed by Wagner [47]. The corresponding (modified) Auger parameter, α , of a given cation or anion in the amorphous oxide film is defined by [47, 48, 49]:

$$\alpha = E_b^{\text{PE}} + E_k^{\text{AE}}, \quad (1)$$

where E_b^{PE} and E_k^{AE} denote the binding energy (BE) and kinetic energy (KE) of an intense core-level photoelectron line and a sharp core-core-core Auger line of a given element in the oxide, respectively.¹ The AP thus refers to an energy difference between a given photoelectron and Auger line and, consequently, the

¹Here it is noted that in the original works by Wagner [48], the Auger parameter, α , was defined by the difference in the *kinetic* energies of the emitted photo- and Auger electrons. However, this value depends on the incident photon source and therefore this original definition of α was soon abandoned. Instead a so-called *modified* Auger parameter, as defined in Eq. (1), was introduced, originally denoted as alpha prime, i.e. α' . Nowadays the modified Auger parameter is the standard and denoted by α .

value of α is independent of the photon source, the defined reference state (e.g. the Fermi level), and possible charging during measurement. For example, a *full* chemical state analysis of both the cations and anions in alumina at *near-constant probing depth* [34] is typically performed by measuring the Al 2p photoelectron and the Al KL₂₃L₂₃ Auger lines to determine the Al Auger parameter ($\alpha_{\text{Al}} = E_{\text{b}}^{\text{Al}2\text{p}} + E_{\text{k}}^{\text{AlKL}_{23}\text{L}_{23}}$), and the O 1s and the O KL₂₃L₂₃ lines to assess the O Auger parameter ($\alpha_{\text{O}} = E_{\text{b}}^{\text{O}1\text{s}} + E_{\text{k}}^{\text{OKL}_{23}\text{L}_{23}}$) [50, 34].

The corresponding (modified) Auger parameter shift, $\Delta\alpha$, between two different chemical states of a given element in the solid [49] can be estimated from the respective difference in the relaxation (or polarization) energy, ΔR :

$$\Delta\alpha = 2\Delta R = 2[\Delta R^{\text{a}} + \Delta R^{\text{ea}}], \quad (2)$$

where ΔR^{a} and ΔR^{ea} correspond to atomic and extra-atomic contributions to the relaxation energy, respectively. The shift ΔR^{a} is due to differences in the valence charge of the core-ionized atom in its initial ground-state (i.e. before) and its final state. If the number of the valence electrons remains constant in the photoemission final state, this contribution can be neglected [49] (as discussed in more detail below). The extra-atomic relaxation energy, R^{ea} , represents the screening of the core-ionized atom by the local density of states of valence electrons around the core-ionized atom. The amount of final-state relaxation provided through this mechanism strongly depends on the electronic polarizability of the nearest-neighbor ligands which constitute the nearest-neighbor coordination sphere (NNCS) around the core-ionized atom, as schematically illustrated in Fig. 1(b). In this regard, it is important to emphasize that any initial-state contributions to the chemical shifts of the respective photoelectron and Auger lines cancel out in the original derivation of Eq. (3). This implies that any shift, $\Delta\alpha$, only probes final-state contributions to the chemical shift, which are very sensitive to tiny changes in the NNCS (i.e. on short-range order) of the core-ionized atom in the solid, as is especially useful for chemical state analysis of defective and amorphous oxide compounds (as for the H-containing *am*-Al₂O₃ ALD films in this study).

For the correct interpretation of Auger parameter shifts of metal cations in compounds, it is essential to distinguish the cases dominated by atomic versus extra-atomic relaxations. A contribution from ΔR^{a} due to electron transfer from neighboring ligands is quite common for late transition metal cations with empty well-localized *d* orbitals [49]. The Auger parameter for metal cations in such compounds would then only weakly depend on the local chemical environment and resemble efficient electronic screening in a metallic state (for which the complete transfer of one free electron from the conduction band to the core-ionized atom is expected). In such cases, the limiting case $R^{\text{a}} \gg R^{\text{ea}}$ with $R^{\text{ea}} = 0$ holds, and a corresponding estimation of R^{a} would require advanced quantum mechanical calculations, as discussed in detail by Moretti [49].

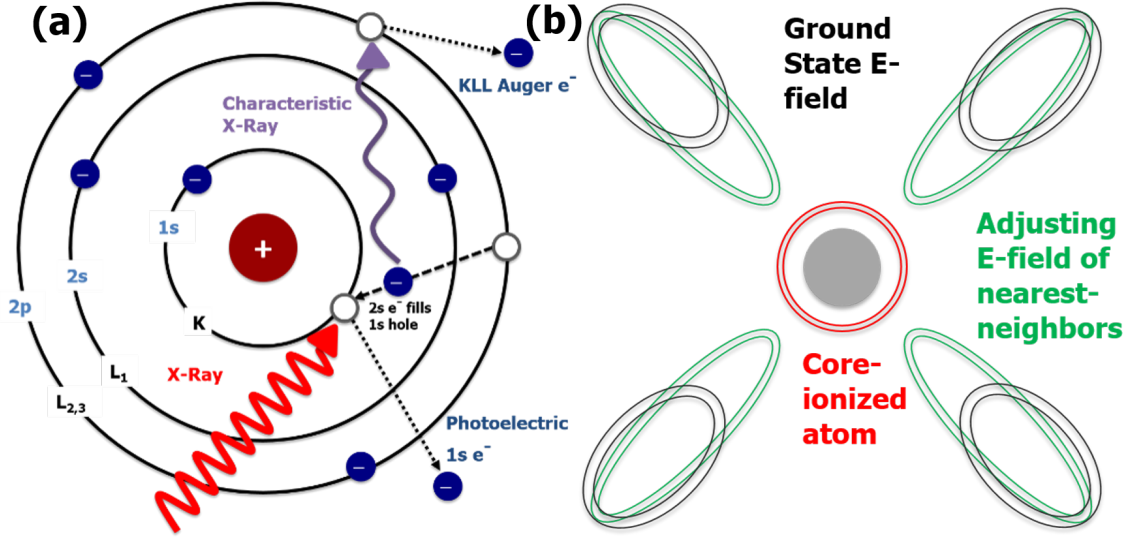


Figure 1: (a) Visualization of the $KL_{23}L_{23}$ Auger process: In a first step, an incoming photon excites a $1s$ core-level photoelectron. The binding energy of this photoelectron is determined by the difference between the incident X-ray energy and the detected kinetic energy of the emitted photoelectron ($E_b^{PE} = h\nu - E_k^{PE}$). The created core hole is then filled by an electron from a higher orbital; this transition releases energy, which ejects a second electron from another orbital, known as the Auger electron. The Auger transition involves three electronic orbitals: the core orbital from which the photoelectron is ejected, the higher-level orbital that fills the core hole, and another higher-level orbital from which the Auger electron is ejected. The Auger electron shown here is denoted as $KL_{23}L_{23}$ (where K denotes the $1s$ shell, L_2 denotes the $2p_{\frac{1}{2}}$ orbital and L_3 denotes the $2p_{\frac{3}{2}}$ orbital). (b) Schematic representation of extra-atomic screening of a core-ionized atom, as governed by the electronic polarizability of its neighboring ligands.

Fortunately, Al oxides, hydroxides, and other Al-O-based compounds are characterized by cation AP values, $\alpha_{Al} = E_b^{2p} + E_k^{KL_{23}L_{23}}$, in the range from 1460 to 1462 eV [51, 52], which are much smaller than the AP value of 1466 eV for Al metal [51, 53]. It is thus safe to assume that ΔR^a in such compounds are dominated by extra-atomic relaxation, i.e., $R^{ea} \gg R^a$ and thus

$$\Delta\alpha = 2\Delta R^{ea} \quad (3)$$

In this limiting case, any measured shift $\Delta\alpha_{Al}$ between two different am - Al_2O_3 polymorphs (e.g. with low and high H-impurity content) is indicative of tiny differences in the NNCS of the core-ionized Al atoms (as defined by bond lengths, bond angles, and coordination number) and/or a change in the (averaged) ligand polarizability; the corresponding difference in extra-atomic relaxation energy can be estimated using relatively simple electrostatic models [49, 54].

It is most appropriate to reference experimentally measured Auger parameter values to the Auger parameter of a single atom without nearest-neighbor ligands, thus representing an atomic gas α_{gas} for which $R_{gas}^{ea} = 0$. This simplifies Eq. (3) to:

$$\alpha - \alpha_{gas} = 2R^{ea}. \quad (4)$$

While an Auger parameter for Al atomic gas is not reported in the literature, Moretti [49] predicted (extrapolated) α_{gas} of 1454.0 eV from the linear relationship between the Al Auger parameter α_{Al} and $(n^2 - 1)/n^2$ for Al metal and for various Al-O-based compounds, where n is the respective refractory index [55]. Using the latter value and those corresponding to Al-O-based compounds, we can estimate R^{ea} in the range of 3-4 eV, highlighting the significant impact of extra-atomic relaxation for efficient electronic screening of a created core-hole by nearest-neighbor ligand polarization.

There is a long-lasting discussion in the literature about the applicability of the oxygen Auger parameters, $\alpha_O = E_b^{O1s} + E_k^{OKL_{23}L_{23}}$ and $\beta_O = E_b^{O1s} + E_k^{OKL_{1}L_{23}}$, since the O $2p$ (and too a much lesser extend the O $2s$) orbital(s) involved in the Auger emission process are delocalized *valence* levels (and not localized core levels), which violates the underlying assumptions in the derivation of Eq. (3) [56, 57, 49]. Nevertheless, previous experimental studies have convincingly demonstrated that oxygen parameter shifts of oxides are actually very sensitive and powerful for tracing e.g. the development of long-range order upon the crystallization of amorphous oxides with increasing temperature [40, 58, 59]. As discussed in Ref. [34], incorporation of H into am - Al_2O_3 ALD films (as grown at relatively low temperatures up to

200°C) only results in a measurable systematic shift of the Al Auger parameter; the O Auger parameter appears unaffected. Therefore, in the following, we focus on the prediction of the Al Auger parameter shift as a function of the H content in *am*-Al₂O₃ ALD films. To this end, we superimpose experimental XPS characterization, high-fidelity atomistic simulations, and the electrostatic theory of extra-atomic relaxation to derive O²⁻ and OH⁻ ligand polarizabilities, as well as to determine the H-distribution in ALD *am*-Al₂O₃ thin films in relation to their key structural building blocks. Our work is the first of its kind that allows for an interpretation of the tiniest Auger parameter shifts in amorphous materials, highlighting the critical role of the ligand polarizability volume and its relation to local charge distribution within the ligand(s).

2. Methods

2.1. Experiment

2.1.1. Atomic Layer Deposition (ALD) of *am*-Al₂O₃

The ALD of amorphous alumina, as detailed in Ref. [34], involves sequential exposure of the substrate to trimethylaluminum (TMA) and water (H₂O), resulting in the formation of a thin *am*-Al₂O₃ film through a series of self-limiting surface reactions. In this ALD cycle, the TMA precursor reacts with surface hydroxyl (OH) groups, leading to the formation of a monolayer of Al-containing species while methane (CH₄) is released as a by-product. Following exposure to TMA, the reaction chamber is purged, and the surface is exposed to water vapor, which reacts with trimethyl groups to further advance *am*-Al₂O₃ layer-by-layer growth and regenerate OH groups on the surface. The process is schematically shown in Fig. 2, highlighting the most likely mechanisms of H-impurity incorporation, as originating from the stochastic nature of surface reactions, inherent surface roughness, and any porosity of the parent substrate. The stochastically occurring surface reactions experience steric hindrance leading to incomplete coverage and reaction of the OH groups, particularly in areas where surface irregularities prevent full precursor saturation. Especially ambient conditions, such as low temperatures and long precursor exposure times, contribute to variations in the reaction extent, leaving behind unreacted OH groups. Although there are many mechanisms by which hydrogen can be incorporated (for example, through unreacted trimethyl groups), these mechanisms have been proven to be less prevalent [33]. In this study, particular attention is given to the impact of the ALD process (growth) temperature on the hydrogen content in the *am*-Al₂O₃ films, as reported in Table 1 by the H/Al-ratio (as experimentally determined in Ref. [34] by combining elastic recoil detection analysis (ERDA) and Rutherford backscattering spectroscopy).² As illustrated in Fig. 2, there is a strong correlation between the quantity of unreacted OH groups and the *am*-Al₂O₃ film density; i.e. the *am*-Al₂O₃ density increases with increasing process temperature, corresponding to a decrease in the H-impurity content and respective H/Al ratio.

Sapphire (α -Al₂O₃) and Bayerite (α -Al(OH)₃) were selected as *crystalline* oxide and hydroxide reference phase, respectively. To this end, a one-side polished α -Al₂O₃[0001] single crystal was purchased from CrysTec GmbH, Germany. The bayerite hydroxide reference was prepared according to the procedure described in Ref. [34]. Bayerite is a trihydroxide with an H/Al ratio of 3 and marks the extreme upper limit of the H/Al spectrum; its density aligns closely with that of the *am*-Al₂O₃ grown at ambient temperature [34]. Sapphire is the most stable bulk alumina oxide and therefore represents the extreme lower end of the H/Al spectrum with a corresponding density of $\rho = 3.9 \text{ g/cm}^3$. All Al cations in sapphire and bayerite are octahedrally coordinated by O and OH ligands, respectively. This makes them exemplary reference materials for the exploration of ligand polarizability effects, as discussed in the following.

²Note that the *am*-Al₂O₃ ALD film grown at 180 °C in Ref. [34] was not simulated in the present study, since its experimental Auger parameter overlaps (within the experimental error) with the ALD film grown at 200 °C. Accordingly, only the *am*-Al₂O₃ ALD film grown at 200 °C was simulated here.

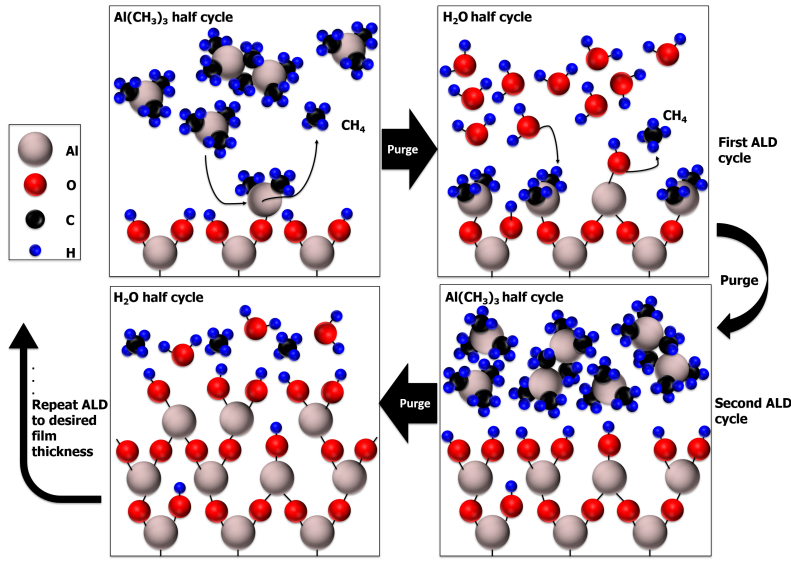


Figure 2: A schematic of the ALD process for *am*-Al₂O₃ using TMA and water precursors.

Table 1: Experimentally determined values and estimated errors for the average densities, H/Al atomic ratios, and measured Auger parameters of the Al cations, for *am*-Al₂O₃ films deposited by ALD, as well as for the crystalline oxide and trihydroxide reference phases, sapphire, and bayerite. See Ref. [34, 60, 61] for more details on the amorphous films and crystalline references. The corresponding densities and H/Al atomic ratios, as simulated in the present study are also listed. A reference value for the Auger parameter of free Al gas of 1454 eV [62] was used to calculate the corresponding Auger parameters shifts, $\Delta\alpha_{\text{Al}}$: see Eq. (4). The final error of the Auger parameter shifts $\Delta\alpha_{\text{Al}}$ of 0.2 eV accounting for the experimental error α_{Al} of 0.1 eV [34] and assumes the same error for the Auger parameter of the free gas. Notably, the corresponding Auger parameter for oxygen does not show a correlation with the H content and has an average value of $\Delta\alpha_{\text{O}} \approx 1039.7 \pm 0.3$ eV, as reported in Ref. [34].

Sample	Density [g/cm ³]		H/Al ratio		$E_{\text{b}}^{2\text{p}}$ [eV]	$E_{\text{k}}^{\text{KL}23\text{L}23}$ [eV]	α_{Al} [eV]	$\Delta\alpha_{\text{Al}}$ [eV]
	Exp.	Sim.	Exp.	Sim.				
Bayerite	2.5	2.5	3	3	74.1	1386.9	1461.0	7.0
Amorphous (25°C)	2.35±0.12	2.29	2±0.05	2	74.7	1386.4	1461.1	7.1
Amorphous (50°C)	2.84±0.11	2.60	1.07±0.05	1	74.6	1387.1	1461.6	7.6
Amorphous (120°C)	3.05±0.06	2.99	0.19±0.01	0.2	74.7	1387.2	1461.9	7.9
Amorphous (150°C)	3.07±0.06	3.00	0.13±0.01	0.125	74.8	1387.3	1462.0	8
Amorphous (200°C)	3.04±0.05	3.01	0.06±0.01	0.0625	74.78	1387.6	1462.4	8.4
Sapphire	3.9	3.9	0	0	73.7	1388.0	1461.7	7.7

2.1.2. XPS/HAXPES Analysis

Combined XPS/HAXPES analysis was performed using a PHI Quantes spectrometer (ULVAC-PHI) equipped with a soft Al-K α (1486.6 eV photon energy) and a hard Cr-K α X-ray source (5414.7 eV photon energy). The linearity of the energy scale of the hemispherical analyzer (i.e., from 0 eV up to 5400 eV) was calibrated according to ISO 15472 by referencing the Au 4f7/2, Ag 3d5/2 and Cu 2p3/2 main peaks to the recommended binding energy (BE) positions of 83.96 eV, 368.21 eV, and 932.62 eV, respectively (as measured in situ for the sputter-cleaned, high-purity metal references using both the soft and hard X-ray source). Charge neutralization during each measurement cycle was accomplished by dual-beam charge neutralization, employing low-energy electron and Ar ion beams (1-V bias, 20- μ A current). First, survey spectra were recorded from all samples with both the soft Al-K α (@50 W) and the hard X-ray Cr-K α source, as reported in Ref. [34]. Next, high-resolution spectra of the Al 2p, O 1s, and C 1s core levels, as well as of the O KLL Auger line, were measured with both X-ray sources using a power of 50 W, a step size of 0.1 eV, and a constant pass energy of 69 eV, resulting in a constant analysis area in the range of 200 - 280 μm^2 . To enhance the signal from the interior of the oxide films and the bulk references, all XPS/HAXPES

measurements were performed at a take-off angle of 90° between the sample surface and the center of the entry lens of the analyzer [63]. The Al KLL Auger transition can only be measured using Cr- $K\alpha$ radiation (adopting the same measurement parameters as above). Notably, a pass energy of 69 eV was carefully selected, since it resulted in a similar energy resolution for both X-ray sources, as evidenced by a constant full-width-at-half-maximum of the Ag 3d_{5/2} peak of 0.9 eV for the XPS and HAXPES analysis. It is further noted that the probing depth of Al 2p photoelectrons excited with Al- $K\alpha$ radiation is approximately the same as the probing depth of the Al KLL Auger electrons, thus ensuring chemical-state analysis at a near constant probing depth of about 9 nm [63].

Data analysis involved peak fitting of the Shirley-background corrected spectra using a single Gaussian-Lorentzian peak component, as fitted to the top of each peak studied (i.e. from approximately 0.7 of the maximum height of the respective peak) using the MultiPak 9.9 software provided by ULVAC-PHI. Since the soft and hard X-ray sources operate with different photon fluxes (and photon energies), their absolute binding energy scales need to be corrected for possible differences in electronic charging, as performed here by aligning the two sets of spectra (as recorded with both sources) to their respective adventitious C 1s peak at 284.7 eV. The correctness of this charge-correction procedure was confirmed by verifying that the photon-source-independent kinetic energy (KE) peak positions of the charge-corrected O KLL spectra from both X-ray sources were identical within ± 0.1 eV. The measured (energy-scale-corrected) Al 2p and Al KLL spectra, as well as the corresponding Auger parameter shifts versus the experimental H/Al ratios (i.e. $\Delta\alpha$ with respect to Al gas) are shown in Figs. 3(a-c), respectively. The thus obtained values of Al 2p BE and Al KLL KE will be further denoted as E_b^{2p} and $E_k^{KL23L23}$, respectively: see Table 1. No clear correlation between $E_b^{Al\ 2p}$ and $E_k^{Al\ KL23L23}$ was found. However, a clear experimental correlation between the H/Al ratio and $\Delta\alpha_{Al}$ is evidenced, which nicely confirms the specific sensitivity of the Auger parameter to final state relaxation effects (see Section 1). In particular, no experimental correlation was obtained between the corresponding Auger parameter for oxygen and the H content, giving an average value of $\Delta\alpha_O = E_b^{O1s} + E_k^{OKLL} \approx 1039.7 \pm 0.3$ eV [34]. As discussed in Ref. [34], only the local chemical state of Al shows a clear trend with increasing ALD deposition temperature (i.e. with decreasing H content). Therefore, in the following, we will focus only on modeling the Al Auger parameter shift with increasing H content in the *am*-Al₂O₃ films.

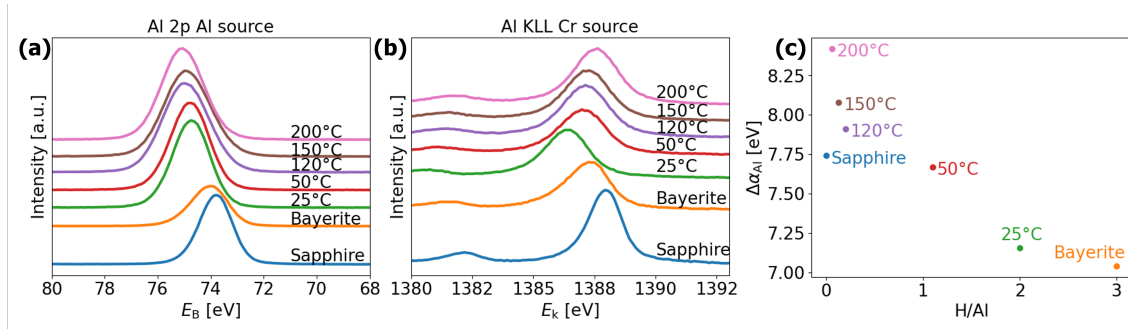


Figure 3: (a) Measured Al 2p spectra (with an inversed BE scale by convention) and (b) Al KLL Auger spectra (with a KE scale) for all ALD and crystalline samples. The spectra’s intensity is represented in arbitrary units (a.u.) and has been vertically stacked for enhanced distinguishability. The measured spectra were charge-corrected by aligning them to their adventitious C 1s peak at 284.7 eV (see Sec. 2.1.2). (c) $\Delta\alpha_{Al}$ as a function of the stoichiometry H/Al.

2.2. Atomistic Simulations

In our study, the methodology used was centered on molecular dynamics (MD) simulations, a technique that is pivotal to probing the atomic-scale interactions and structural nuances of materials. The primary focus was to elucidate the effects of hydrogen incorporation within amorphous alumina films on the corresponding experimentally measured Auger parameter shifts. MD simulations were carried out using Large-scale Atomic/Molecular Massively Parallel Simulator (LAMMPS) [64]. In 0 K calculations, the conjugate gradient method was used to obtain fully relaxed samples. At higher temperatures, the Nose-Hoover thermostat and the Parinello-Rahman barostats were used for temperature and pressure control with damping coefficients of 0.05 ps and 0.5 ps, respectively. The lower-than-default timestep was set to 0.5 fs, to avoid artifacts related to unrealistic hydrogen mobility in amorphous surface structures, and to ensure proper equipartition between different degrees of freedom in the system [65]. Periodic boundary conditions were applied along all dimensions to model bulk phases, excluding surface effects.

After the simulation phase, structural adjustments and analyzes were performed using pymatgen [66],

Atomic Simulation Environment (ASE) [67], and the OViTo visualization tool [68]. ASE and pymatgen offer a robust framework for manipulating atomic simulations, enabling straightforward structure modifications, property calculations, and result visualizations. In contrast, OViTo provides sophisticated visualization and analysis capabilities, especially through its Python interface, making it possible to render and analyze complex atomic structures in an intuitive and detailed manner.

For MD simulations, a sophisticated universal graph neural network potential (NNP), specifically Preferred Potential (PFP) [69], was used. We recently demonstrated the applicability of this type of graph NNPs for the accurate modeling of amorphous alumina [70]. PFP stands out because of its ability to simulate a broad spectrum of molecular and crystalline systems, extending its utility to uncharted materials. It supports simulations that involve combinations of up to 72 elements, supported by a comprehensive training dataset comprising more than 32 million structures consistently derived from high-quality density functional theory (DFT) calculations [71]. As with any other potential, its applicability to the system and property of interest is first tested and justified, as discussed in the Appendix [Appendix A](#). After the inclusion of Van der Waals dispersion correction, the potential accurately reproduces the structures and properties of reference crystalline phases and liquid alumina.

2.2.1. Simulation Procedure of Amorphous Alumina Polymorphs

The simulation of different amorphous oxide polymorphs by atomistic simulations, which align well with experiments, is a very challenging problem to solve. Firstly, significant uncertainty is present in the experimental determination of the chemistry, structure and properties of different amorphous oxide polymorphs, as produced by different fabrication methods: e.g. by thermal oxidation or anodization of pure metals [39, 40, 72], by magnetron sputtering [73, 74], or by ALD [34, 33]. Secondly, as discussed in Section 1, most analytical methods have limitations for resolving the local chemical states (i.e. the NNCSs) of the constituent ions in amorphous phases. The incorporation of hydrogen in such amorphous structures further complicates the detailed chemical and structural experimental analysis, as most techniques can trace light elements, such as H, only indirectly through their chemical and/or structural induced changes. Thirdly, *from the modeling side*, there is inherent uncertainty associated with the atomistic simulation procedures of amorphous structures, as commonly performed through melt quenching [75]. In the melt quenching method, the resulting structure will depend heavily on fabrication parameters such as the annealing temperature, the duration of the annealing, and the quenching rate [75]. Additional degrees of freedom include the choice of time step, thermostat, and barostat types and parameters, and most importantly the choice of the interatomic interaction model. Regarding the latter, even state-of-the-art neural network potentials can be only as good as the underlying *ab initio* data used in their training [70]. For example, metal oxide systems like amorphous alumina in which nominal charge neutrality is not preserved (thus having charged defects) fall outside the purview of classical Density Functional Theory (DFT) calculations employing the PBE level of accuracy [76] - the level used for training the PFP model. Although there are no formal restrictions on the system composition/stoichiometry in the PFP model due to the exclusion of atomic charges from the energy and forces estimation, we enforce the nominal charge neutrality in this work to increase the reliability of our calculations even if it means having minor deviations from experimentally derived stoichiometries for ALD aluminas.

In the first attempt, amorphous alumina polymorphs with different H contents were simulated using the traditional melt quenching procedure. Specifically, we started with a sapphire crystal, heated it beyond its melting point, annealed it until the structural factor stopped changing, and quenched it to room temperature with all the steps done at zero pressure. To reach the targeted H content from experiment, we tried to randomly introduce H atoms into liquid or amorphous alumina, ensuring that they are positioned at a reasonable distance from the surrounding atoms. To maintain charge neutrality within the modeled systems, Al atoms were randomly removed in proportion to the number of inserted H atoms, adhering to a ratio of three H atoms for every Al atom removed. However, for H/Al ratios >1 , the random insertion of hydrogen resulted in proximal H atoms forming H_2 molecules that normally should not be present at any stages of the ALD process [34, 33]. Unfortunately, this issue could only be partially mitigated by selecting various random starting configurations. Moreover, if H is inserted into the liquid alumina before quenching, water molecules can emerge even at a low H content. Although water is an essential part of the ALD process, subsequent XPS analysis of ALD alumina samples did not show any signs of residual water embedded in the structure [34]. We thus concluded that the traditional melt quenching procedure is not suited to generate representative amorphous alumina polymorphs with different H-contents, as observed in the experiment.

Therefore, a *novel simulation approach* was attempted to simulate amorphous oxide polymorphs with different H contents, while also ensuring a good match with the experimental densities. Based on experimental knowledge that H atoms in amorphous oxides strongly interact with oxygen anions to form hydroxyl ligands [77, 34], H atoms were not randomly inserted into the simulation samples, but instead embedded as hydroxyl groups from the start of the simulations. Figure 4 provides a schematic overview of this comprehensive procedure, illustrating the sequential steps undertaken to achieve amorphous alumina

polymorphs with specific H/Al ratios and respective densities, which are consistent with the experiment. To this end, the Al-trihydroxide phase, bayerite, was adopted as the starting crystalline structure. The OH groups and neighboring H atoms were then randomly removed, mimicking the dehydration of bayerite. The removal of equal amounts of OH and H pairs ensured charge neutrality, while the resulting H/Al ratio was matched to the experiment by adjusting the number of removed pairs (see Table 1). Next, in the first equilibration step, the dimensions of the artificially constructed defective bayerite structure were scaled to a density that was about 10% higher than the respective experimental density to promote the interaction of neighboring Al and O atoms with broken bonds. A subsequent second equilibration step at the corresponding experimental ALD temperature then allowed the system to establish new bonds, as accompanied by a further densification towards the experimental density. The second equilibration stage lasted 50 ps at the corresponding experimental ALD temperature, as detailed in Table 1. This phase of equilibration drove the transition of the artificially constructed and structurally unstable, highly defective bayerite structure to an amorphous state. Subsequently, the amorphous structure was quenched from the ALD temperature to $T_E = 300$ K for another 50 ps. During this quenching phase, all six dimensions of the cell were allowed to relax independently to zero pressure. Following the quenching process, a further equilibration period of 50 ps at $T_E = 300$ K was conducted, during which the cell dimensions were meticulously measured and averaged. The culmination of this procedure was a final production run executed at $T_E = 300$ K, with cell dimensions and tilt angles fixed to the average values. Scripts and trajectories are publicly available at materialscloud.org. [78]. The resulting densities are reported in Table 1, demonstrating excellent agreement between the densities predicted from simulations and measured experimentally, highlighting the reliability of PFP. A comparable impressive agreement is achieved for the crystalline reference structures using the two equilibration stages performed at $T_E = 300$ K. In the final production run, 1000 snapshots (i.e. every 100 timesteps) of each system are generated for the time-averaged analysis of sample structures accounting for thermal noise.

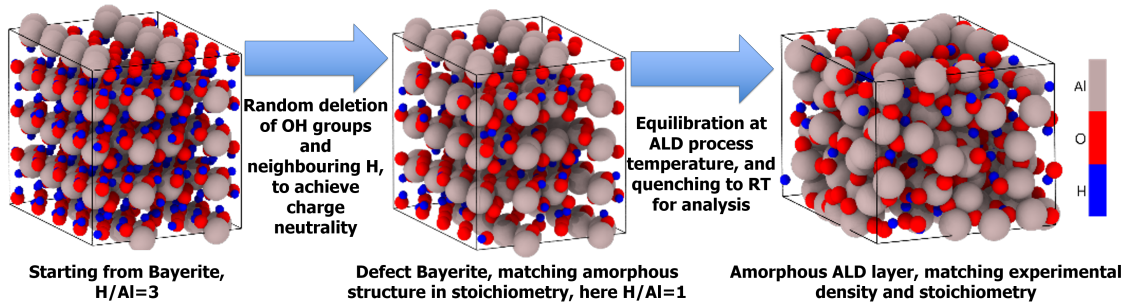


Figure 4: A schematic representation of the novel simulation method employed to generate amorphous oxide polymorphs with different H-contents and densities by starting from an artificially constructed, highly defective bayerite structure, while maintaining nominal charge neutrality.

2.3. Structural Analysis of Simulated Amorphous Alumina Polymorphs

Fig. 5 presents a comprehensive analysis of six different amorphous oxide polymorphs with specific H/Al-ratios and densities, as aligned with the experiment (see Table 1). A visualization of the simulated structures is shown in Fig. 5(a). The corresponding radial distribution functions (RDFs) from $r = 0 - 10$ Å, as well as the bond-specific Al-O and O-H partial radial distribution functions (PRDFs), from $r = 0 - 3$ Å are shown in Figs. 5(b-c). Details on the respective cell dimensions are given in Table B2. The crystalline α - Al_2O_3 reference (sapphire) is shown at the top left with all Al^{3+} cations in 6-fold octahedral coordination with O^{2-} . The crystalline α - $\text{Al}(\text{OH})_3$ trihydroxide reference (bayerite) is composed of a stacking of two planes of close-packed OH^- with Al^{3+} in octahedral coordination sandwiched between them. The amorphous structures generated at a process temperature of 25°C display a more complex distribution of nearly equal fractions of 6-fold (violet), 5-fold (green) and 4-fold (yellow) $[\text{AlO}_n]$ polyhedra, in excellent agreement with experimental findings [79, 80, 81, 82, 83, 84]. This implies that the artificially created defective bayerite structures (see Section 2.2) transform into an amorphous state during thermal equilibrium at the respective ALD growth temperatures. Comparison of the amorphous alumina polymorphs with different H/Al ratios and densities (corresponding to ALD temperatures of 50°C, 120°C, 150°C, and 200°C, respectively; as quenched to $T_E = 300$ K) reveal the following trend: an increase of the ALD processing temperature results in a lower hydrogen content, which is accompanied by a decrease of the proportion of 6-fold $[\text{AlO}_n]$ polyhedra, with 5-fold NNCS predominating over 4-fold ones.

The total radial distribution function, $g(r)$, in Fig. 5(b) evidences long-range order for crystalline sapphire and bayerite, whereas the amorphous polymorphs only exhibit short-range order (i.e. a broad

first nearest-neighbor peak only). Only bayerite shows a split of the O-O peak due to its two distinctly different oxygen environments [85]. The partial Al-O radial distribution function, $g_{\text{Al-O}}(r)$, in Fig. 5(c) (for $r = 1 - 3 \text{ \AA}$) displays a fairly narrow spread of the Al-O bond lengths for the different amorphous polymorphs; the first neighbor peak shifts from 1.93 \AA to 1.85 \AA when moving from the crystalline references to the amorphous polymorphs. Accordingly, a respective coordination cutoff radius of 2.2 \AA (position of the well after the first nearest neighbor peaks) was selected for further structural analysis of the 6-fold, 5-fold and 4-fold $[\text{AlO}_4]$ coordination spheres (see black line). The partial O-H radial distribution function $g_{\text{O-H}}(r)$ in Fig. 5 (for $r = 0 - 2.1 \text{ \AA}$) indicates a constant O-H bond length for all structures studied, in accordance with the presumed (covalent) bonding of atomic H atoms to O ions forming hydroxyl groups. Accordingly, a respective coordination cutoff radius of 1.2 \AA was adopted in Section 3.1 for determining the fraction of OH-ligands, f_{OH} , and O-ligands, f_{O} , in each amorphous polymorph (see vertical black line).

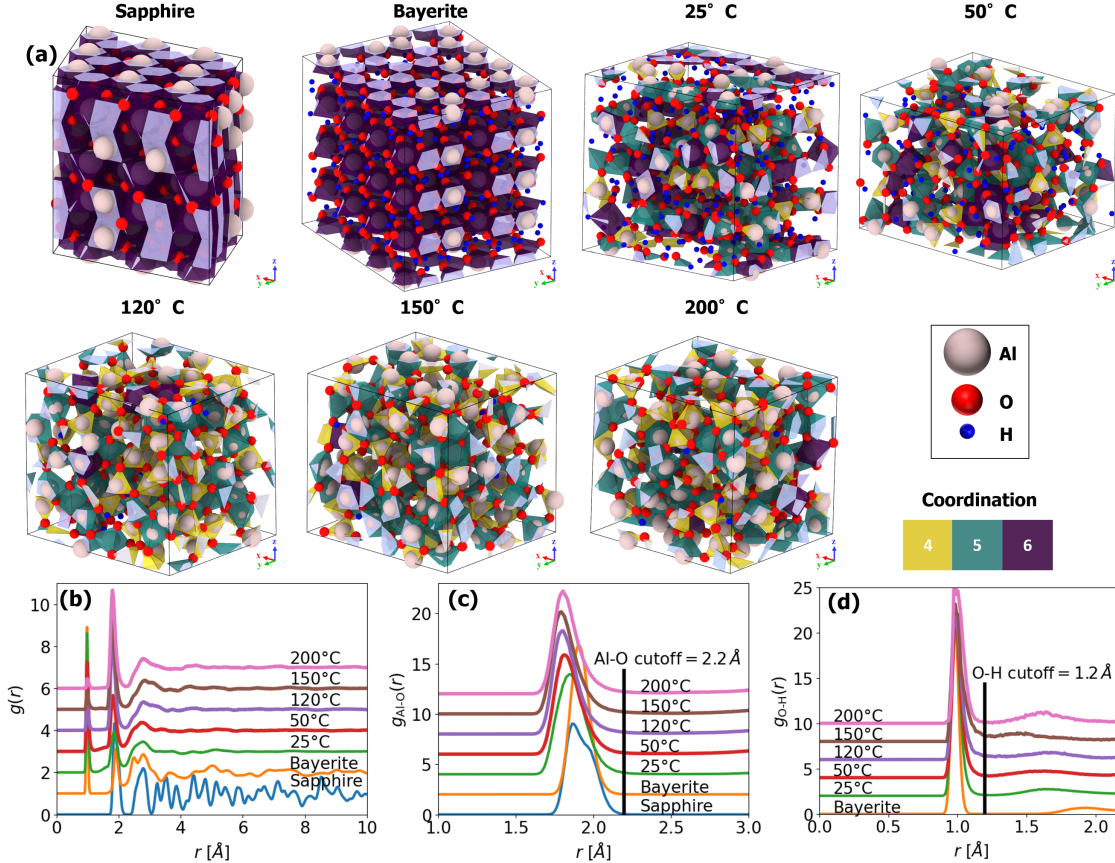


Figure 5: (a) Analysis of the six amorphous alumina polymorphs with different H/Al-ratios and densities (corresponding to different ALD temperatures, as equilibrated at $T_E = 300 \text{ K}$), as well as of crystalline sapphire and bayerite (see Table 1). The corresponding simulation cell dimensions and numbers of atoms are given in Appendix Appendix B. (b) The total radial distribution functions, $g(r)$, evidencing long-range order in the crystalline phases and short-range order in the amorphous polymorphs. (c) The partial Al-O radial distribution function, $g_{\text{Al-O}}(r)$, with an indication of the selected cutoff radius (black line) for determining the fractions of O and OH ligands in Section 3.1. (d) The partial O-H radial distribution function, $g_{\text{O-H}}(r)$, evidencing preferential bonding of atomic H to O anions to form hydroxyl groups with uniform O-H bond lengths. This justifies the selected hydroxyl cut-off radius, as indicated by the black line

2.4. Principles of the applied electrostatic models

Historically, researchers have proposed numerous empirical correlations to link the Auger parameter shift to the electronic polarizability of the chemical environment surrounding the core-ionized atom [86, 87, 88]. Moretti [89] developed a simple electrostatic model to calculate the extra-atomic polarization energy, R^{ea} , of the first-neighbor ligand shell around core-ionized cations and thereby the resulting Auger parameter shift $\Delta\alpha = 2R^{\text{ea}}$. In the proposed model, the final-state polarization process is characterized by classical electrostatic calculations. These calculations aim to determine the total electric field experienced by the

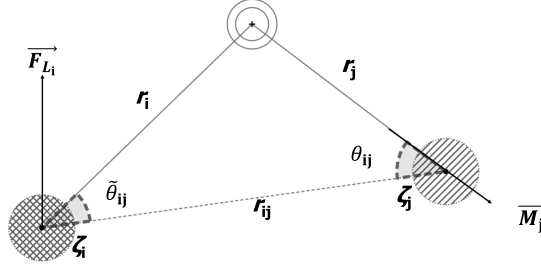


Figure 6: Diagram illustrating the electrostatic approach for the computation of polarization energy. The model envisages a plane encapsulating the atom with a core hole alongside two adjacent ligands, labeled i and j . Employing electrostatic theory, the formulated expressions elucidate the electric field at ligand i attributable to the induced dipoles on ligand j (M_j) and the local field at ligand i . As adopted from Ref. [90].

ligands upon the creation of a core hole in a central atom. This total field includes contributions from both the central positive charge of the core-ionized atom and the electric fields resulting from induced dipoles on the ligands within the closest-neighbor shell [49]. Although a strong approximation resulted from the analysis of molecular systems, the nearest-neighbors models have been shown to work equally well for crystalline and amorphous solids [49]. The interactions between the core-ionized atom and its nearest-neighbors are encapsulated by the electronic polarizability volumes (in \AA^3), denoted as ζ_i . The parameter ζ_i serves to quantify the magnitude of the dipole moment

$$M_i = 4\pi\epsilon_0\zeta_i F_{L_i} \quad (5)$$

induced within the i^{th} ligand as a direct response to the electric field, F_{L_i} , generated by the core-ionized atom (see Fig. 6), with ϵ_0 being the dielectric constant. This selective focus on the first coordination shell and the corresponding electronic polarizabilities provides a nuanced understanding of the electrostatic interactions facilitated by the presence of a core hole, highlighting the utility of the model in the study of the electronic structure and bonding properties of materials.

2.4.1. Complete model formulation

Moretti [49] developed a comprehensive electrostatic model that uses a series of geometric assumptions capable of predicting the extra-atomic relaxation energy. The model is concisely captured by the equation:

$$\Delta\alpha = 2R^{\text{ea}} = 14.4 \sum_i \zeta_i / r_i^2 \sum_j C_{ij} / r_j^2 \quad (6)$$

where ζ_i symbolizes the electronic polarizability volume of the i^{th} ligand, and 14.4 is the scaling factor to get the eV units. In this expression, r_i and r_j refer to the distances from the core-ionized atom to the i^{th} and j^{th} ligand, respectively. The spatial distribution of these distances and related parameters are depicted in Fig. 6. C_{ij} contains all further geometric information to calculate $\Delta\alpha$ and is given by [49]

$$C = B^{-1} \quad (7)$$

with

$$B_{ij} = \begin{cases} 1, & \text{if } i = j. \\ \zeta_j T_{ij} / (r_i \cos \tilde{\theta}_{ij} + r_j \cos \theta_{ij})^3, & \text{otherwise.} \end{cases} \quad (8)$$

and T_{ij} given as

$$T_{ij} = \cos \theta_{ij} \sin \tilde{\theta}_{ij} \sin (\tilde{\theta}_{ij} + \theta_{ij}) + (3 \cos^2 \theta_{ij} - 1) \cos (\tilde{\theta}_{ij} + \theta_{ij}). \quad (9)$$

Within the framework of the aforementioned equations, the terms θ_{ij} and $\tilde{\theta}_{ij}$ play a pivotal role in quantifying the angular relationship between ligands and the core-ionized atom, as visualized in Fig. 6. Specifically, these parameters capture the spatial orientation of the ligand relative to another ligand and the core-ionized atom, thereby reflecting the geometric nuances of their interactions. Consequently, T_{ij} emerges as a crucial term designed to encapsulate the local environmental characteristics of an atom, employing geometric functions to provide a comprehensive description. This approach allows for a detailed assessment of how the spatial arrangement and angular disposition of ligands influence the electrostatic potential and, by extension, the electrostatic properties of the system under study.

2.4.2. Simplified model formulation

Building upon the comprehensive framework for predicting ΔR^{ea} with the use of T_{ij} , Moretti also introduced a simplified version of the model. This streamlined approach, detailed in his seminal works [89, 90, 49], relies on specific assumptions relevant to ordered materials exhibiting high symmetry. Central to this simplification is the postulate that the angular relations between the ligands and the core-ionized atom are uniform, denoted as $\theta_{ij} = \hat{\theta}_{ij}$, and that the electronic polarizabilities of all ligands are equal, $\zeta_i = \zeta_j = \zeta$. Additionally, it assumes that the distances from the core-ionized atom to all ligands are identical, represented by $r_i = r_j = r$. Under these conditions, the model yields a more accessible expression for estimating the extra atomic relaxation energy, encapsulating the effects of symmetry and uniformity in the material’s structure on its electrostatic properties. The simplified model for the Auger parameter shift with respect to the gas phase is defined as:

$$\Delta\alpha = 2R^{\text{ea}} = \frac{14.4n\zeta}{rD\zeta + r^4} \quad (10)$$

where the factor

$$D = \sum_{j \neq i} \frac{1 + \cos^2 \theta_{ij}}{8 \cos^3 \theta_{ij}} \quad (11)$$

occupies a central role in the computation of Auger parameter shifts, primarily because it accounts for the dipole-dipole repulsion among the induced dipoles on the ligands.

In the context of atomistic simulations targeting non-symmetric solids with variable coordination environments, as for the amorphous alumina polymorphs in the present study, we adopt the methodology wherein the relationship delineated in Eq. (10) is presumed to be applicable. This applicability is facilitated through the employment of time- and structure-averaged values for all pertinent geometric properties derived from the simulation’s production runs. For each sample with different H content, we account for the different fractions of the O^{2-} and OH^- nearest-neighbor ligands with polarizabilities ζ_{O} and ζ_{OH} , respectively, by assuming that the average polarizability simply follows the rule of mixtures:

$$\zeta = \zeta_{\text{O}}(1 - f_{\text{OH}}) + \zeta_{\text{OH}}f_{\text{OH}}, \quad (12)$$

where f_{OH} is the time-averaged fraction of OH^- nearest-neighbor ligands.

2.5. Bayesian optimization of ligand polarizabilities

Bayesian optimization is a powerful technique for optimizing objective functions that are expensive to evaluate. It operates by constructing a posterior distribution of functions, typically using a Gaussian process, which serves as a probabilistic model for predicting the objective function’s outputs based on its inputs. As observations accumulate, this posterior distribution is refined, enhancing the algorithm’s capacity to discern promising regions within the parameter space for further exploration. For a comprehensive understanding of this method, readers are referred to the relevant literature [91, 92, 93].

By applying the analysis based on Eq. (12) or Eq. (10) to 1000 snapshots from the MD production run for each sample, we can compare the predicted time- and structure-averaged Al Auger parameter shifts, $\Delta\alpha_{\text{Al,pred}}$, with our experimentally-measured data, $\Delta\alpha_{\text{Al,exp}}$, as presented in Table 1. This formulation enables the establishment of an acquisition function, F , which solely depends on ζ_{OH} and ζ_{O} , expressed as:

$$F = - \sum_{\text{samples}} (\Delta\alpha_{\text{Al,exp}} - \Delta\alpha_{\text{Al,pred}}(\zeta_{\text{OH}}, \zeta_{\text{O}}))^2. \quad (13)$$

This function F is then maximized using Bayesian optimization (with the Python code [94]) within the experimentally reported limits for the polarizability volumes of metal oxides between 0.9 and 3.2 \AA^3 set equal for both ligands [95].

2.6. *Ab initio* calculations

To interpret the extracted polarizabilities, Density Functional Theory (DFT) calculations with ground-state Bader charge analyses were performed in reference crystalline compounds and amorphous samples using Vienna *Ab initio* Simulation Package (VASP) software (version 6.3.0) [96, 97, 98, 99]. Core electronic interactions were modeled using the projector augmented-wave (PAW) method, which provides an accurate

representation of core electrons and treats valence electrons within a plane-wave basis [100, 101]. The exchange-correlation energy was approximated by the generalized gradient approximation (GGA) [102], employing the PBE functional to balance computational efficiency with precision in material property predictions [103]. Brillouin zone sampling was restricted to the Γ -point only, which is a reasonable assumption due to the relatively large simulation cells (over 300 atoms) used in this work.

The treatment of Van der Waals interactions, crucial for precise intermolecular force calculations, was incorporated through the DFT+D3 method [104]. Bader charge analysis was conducted to determine atomic charges using algorithms and methods developed by Henkelman *et al.* [105, 106, 107, 108]. The calculation of Bader charges plays a crucial role in understanding and predicting the chemical shifts observed in spectroscopic methods like XPS and Auger spectroscopy. By establishing a linear relationship between the Auger parameter shift and the ground state Bader valence charge, researchers can now separate the initial and final state effects that co-determine core electron binding energy shifts [109]. This method provides a robust framework for rationalizing the variance in binding and Auger energies across different compounds, particularly halides, and chalcogenides of Ba, Zn, Pb, and Cu [110]. Future research can leverage this approach to quantify and isolate factors affecting the kinetic energies of core photoelectrons, enhancing the accuracy of spectroscopic analysis and potentially revealing unique electronic properties of materials, including semiconductor behaviors.

The initial structures for calculating Bader charges were derived from the last snapshot of the MD production simulations with PFP, which then undergoes the relaxation of the ionic positions using VASP while maintaining the shape and size of the simulation box. This allows us to remove thermal fluctuations before analysis while retaining the $T_E = 300$ K density of each system. Due to the large size of the simulation box, the 25°C ALD sample analysis was not used with DFT. For the same reason, a smaller cell for Bayerite with 112 atoms instead of 896 atoms is introduced and used for the Bader charge analysis.

3. Results and Discussion

3.1. Model predictions using the simplified electrostatic model

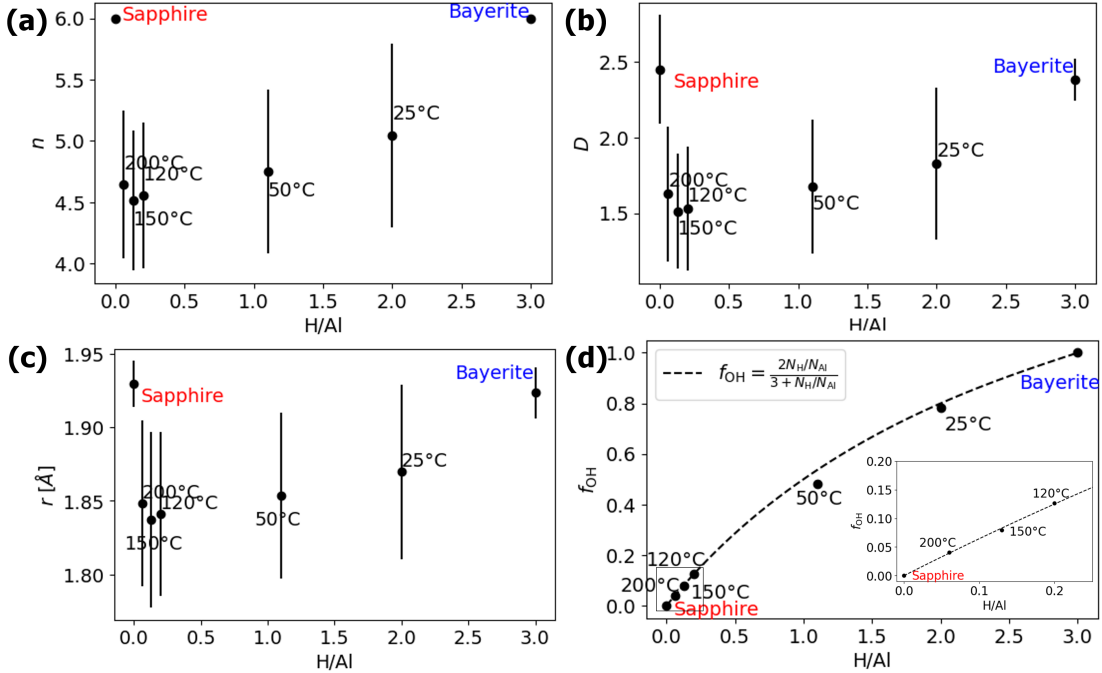


Figure 7: Average structural parameters (with corresponding standard deviation) as extracted from the Al NNCS of the simulated amorphous alumina polymorphs, as well as of the crystalline oxide and hydroxide reference phases: (a) The average nearest-neighbor coordination number of Al cations by O(H) ligands, n , (b) The average geometric factor, D . (c) The average Al-O bond length, r , (d) The average fraction of OH ligands, f_{OH} (as determined using a cutoff distance of 1.2 Å). The structural parameters are plotted as function of the H/Al-ratios, as reported in Table 1.

Fig. 7 shows the average structural parameters n , D , r and f_{OH} (with their corresponding standard deviations) versus the H/Al-ratio, as extracted from the simulated structures of the amorphous alumina polymorphs, as well as of the crystalline oxide and hydroxide reference phases. The average nearest-neighbor coordination number of Al cations by O(H) ligands, n , in Fig. 7(a) reveals a clear separation between the crystalline reference phases and the amorphous polymorphs. For sapphire and bayerite, all Al cations are in 6-fold coordination with O and OH ligands, respectively. The amorphous polymorphs result in lower average coordination numbers, which also exhibit a relatively large spread (i.e. a large standard deviation). This can be attributed to the characteristic network of randomly interconnected and partially distorted 4-fold, 5-fold and 6-fold $[AlO_n]$ polyhedral building blocks in *am*- Al_2O_3 [79, 80, 81, 82, 83, 84, 111]. The average n -value for the amorphous polymorphs decreases with decreasing H content (i.e. with increasing T), which is mainly due to a decreasing fraction of 6-fold NNCS (as compared to 4-fold and 5-fold NNCS; see Fig. 5(a)). This simulation result is in excellent agreement with the experiment showing that $[AlO_6]$ polyhedra convert to $[AlO_5]$ and $[AlO_4]$ polyhedra when releasing OH ligands and/or H_2O during thermal annealing [82]. As discussed in Ref. [82], hydroxide ligands in Al NNCS can convert to bridging O-H...O species, two of which can react to form a single Al-O-Al bridging configuration, thereby reducing the average coordination number of Al. Notably, this process is already thermally activated at temperatures as low as 200 °C [82], which nicely coincides with the onset temperature for the crystallization of *am*- Al_2O_3 in the range of 180 - 200 °C [112, 72].

Fig. 7(b) shows the corresponding average geometrical factors, D , as a function of the H/Al ratio. The crystalline phases exhibit the highest D -value close to 2.37, as calculated for perfect octahedral (6-fold) building blocks by Moretti [90]. The amorphous polymorphs all have a lower average D value due to the coexistence of 4-fold and 5-fold (besides 6-fold) NNCS. For all amorphous polymorphs, the average geometric factor exceeds $D > 1.15$, as calculated for a perfect tetrahedral (4-fold) NNCS [90]. In this regard,

it is observed that some $[\text{AlO}_n]$ NNCS in $am\text{-Al}_2\text{O}_3$, and even in well-defined crystalline reference phases (such as $\gamma\text{-Al}_2\text{O}_3$ and even $\alpha\text{-Al}_2\text{O}_3$) will be partially distorted [79, 82, 111], which induces spread in D (and also of r ; see below). As demonstrated in Appendix Appendix C, the established relation between D and n for the amorphous structures studied can be approximated by $D = 0.07n^2$, which further simplifies Eq. (10) to:

$$\Delta\alpha = 2R^{\text{ea}} \approx \frac{14.4n\zeta}{0.07n^2\zeta r + r^4} \quad (14)$$

Fig. 7(c) shows the average radius, r , between the Al cations and their nearest-neighbor O(H) ligands (i.e. the average Al-O bond length) as a function of the H/Al ratio. The average Al-O bond lengths for sapphire and bayerite are very similar, which highlights the structural similarity of the long-range ordered $[\text{AlO}_6]$ and $[\text{Al}(\text{OH})_6]$ NNCS in both phases. The amorphous polymorphs exhibit considerably lower average Al-O bond lengths (with a much larger variation), which complies well with the smaller average Al-O bond length for 4-fold (and presumably also of 5-fold) $[\text{AlO}_n]$ NNCS as compared to 6-fold NNCS [113]. The bond lengths in the range of 1.84 - 1.87 Å, as extracted from the simulated amorphous structures, are in excellent agreement with the experimental Al-O bond lengths for $am\text{-Al}_2\text{O}_3$ ALD films in the range of 1.81 - 1.84 Å [114]. The amorphous polymorphs show a gradual decrease in the average length of the Al-O bond with decreasing H content (i.e. with increasing T_{ALD}), in accordance with a simultaneous decrease in n , as discussed above. Consequently, the average Al-O bond distance, r , and the average coordination number, n , show a strong correlation, which can be expressed in the empirical power law as $r = 1.4n^{1/6}$ (see Appendix Appendix C).

The observation that sapphire and bayerite have near identical values of D , r , and n , but display the 0.7 eV difference in their Al Auger parameter shifts (compare Fig. 7(a-c), Table 1 and Fig. 3(c)) emphasizes strikingly different electronic polarizability for the O and OH ligands, respectively. The lower electronic polarizability of OH ligands compared to O ligands can be visualized by calculating the charge isosurfaces of O in sapphire and bayerite (by *ab initio* calculations; see Methods), as shown in Figs. 8(a),(b) respectively. It follows that for sapphire, the valence charge of O is near spherical and slightly stretching towards three Al atoms, forming a trigonally elongated spherical shape typical for each O ligand. In contrast, for bayerite, there is a notable shift in the O valence charge distribution towards the H atom (due to the formation of covalent O-H hydroxyl bonds), resulting in a more drop-like shape of the charge density for OH ligands. Consequently, $\zeta_{\text{O}} > \zeta_{\text{OH}}$ since the valence electron density of a nearest-neighbor OH ligand next to the core-ionized Al cation is reduced, leading to reduced non-local screening ability and polarizability.

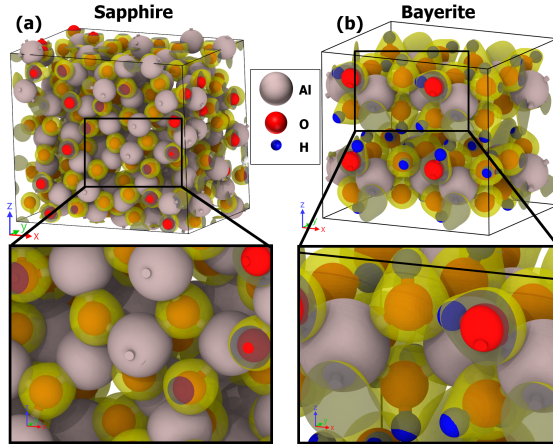


Figure 8: Isosurfaces in the crystalline reference phases (a) Sapphire and (b) Bayerite, as derived from *ab initio* calculations (see Methods). The isosurface level used is $0.5 \text{ e}/\text{\AA}^3$.

Assuming that the average ligand polarizability follows the rule of mixture (see Eq. (12) and subsequent discussion), the fractions of OH ligands derived from the simulated structures are plotted as a function of the H/Al-content in Fig. 7(d). The strict constraint of overall charge neutrality demands the following relation between the fractions of cations and anions: $3N_{\text{Al}} - 2N_{\text{O}} - N_{\text{OH}} = 0$. If all hydrogen is assumed to react with O to form OH ligands (i.e. $N_{\text{OH}} = N_{\text{H}}$) [115, 77, 34], the following relation between the fraction of OH ligands and the H/Al ratio is obtained:

$$f_{\text{OH}} = \frac{N_{\text{OH}}}{N_{\text{O}} + N_{\text{OH}}} = \frac{2N_{\text{H}}/N_{\text{Al}}}{3 + N_{\text{H}}/N_{\text{Al}}} \quad (15)$$

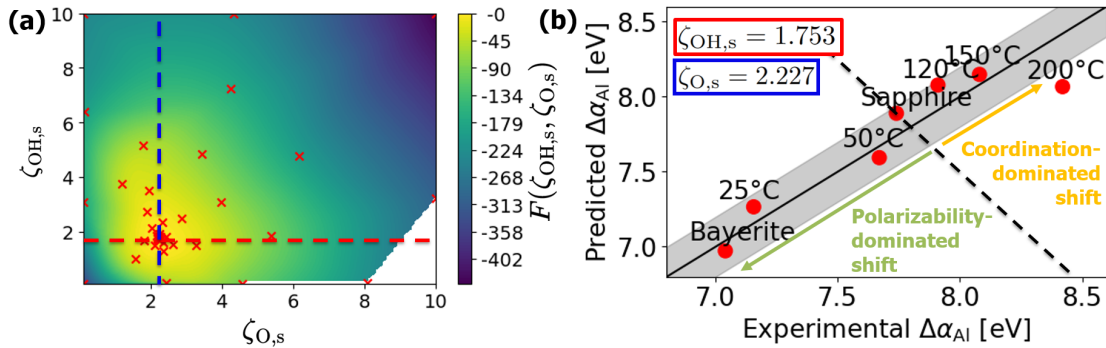


Figure 9: Visualization of the Bayesian optimization process: (a) Application to the simplified model, involving 104 optimization steps maximizing function F . (b) The shift in the Al Auger Parameter, $\Delta\alpha_{\text{Al},s}$, as calculated using the simplified model, versus the respective experimentally determined value, $\Delta\alpha_{\text{Al}}$. Points lying on the diagonal black line represent perfect agreement with experimental data. The surrounding grey area delineates the empirical experimental error margin of ± 0.2 eV.

The dashed line in Fig. 7(d) indicates this relationship and shows very good agreement with the simulated data points, which supports our assumption that H preferentially bonds to O ligands of the Al cations, thereby reducing the average number of O ligands with respect to OH ligands. Small deviations from the ideal relationship can be attributed to the dynamic nature of O-H bonds caused by thermal fluctuations, leading to a possible overestimation of the fraction of hydroxyl groups due to the co-existence of "non-bonded" (i.e. more mobile) interstitial protons [116, 77] (as discussed in more detail below).

Next, the unknown polarizabilities of O and OH ligands were derived using a Bayesian optimization process employing the extracted average structural parameters pertaining to Fig. 7(a-d). As discussed in Section 2.5, the Bayesian method benefits from the computation of property averages across all simulation trajectories, thus streamlining the optimization process and maximizing function F . Fig. 9(a) demonstrates that the mixed exploration/exploitation procedure in the Bayesian optimization of ζ_{O} and ζ_{OH} rapidly converges to values within the range of 0.9 - 3.2 \AA^3 , in agreement with experiment [95, 58]. The optimization process for the simplified model, as illustrated in Fig. 9(a), results in optimized fitting parameter values of $\zeta_{\text{OH},s} = 1.753 \text{ \AA}^3$ and $\zeta_{\text{O},s} = 2.227 \text{ \AA}^3$, which match well a rough empirical estimate of 2 \AA^3 for free-standing OH^- and O^{2-} ligand polarizabilities in Ref. [117].

In a final step, the Al Auger parameter shift was calculated from Eq. (10) using the optimized $\zeta_{\text{O},s}$ and $\zeta_{\text{OH},s}$ ligand polarizabilities. The thus predicted values, $\Delta\alpha_{\text{Al},s}$, are plotted as a function of the measured Auger parameter shifts, $\Delta\alpha_{\text{Al}}$, in Fig. 9(b), evidencing an excellent agreement between experiment and theoretical prediction (even for the simplified model used here). Despite the demonstrated success, it is important to note that electrostatic models typically assume that extra-atomic relaxation is only influenced by the nearest-neighbor ligands with well-defined polarizabilities, independent of their environment. To validate this assumption, additional DFT calculations were performed to determine the charge densities of the valence electrons in Al, O, and H atoms, and their corresponding Bader charges (q_{B}). Figs. 10(a) and 10(b) show visualizations of the isosurfaces around O in samples with H/Al ratios of 1 and 0.013, respectively (for which the calculated $\Delta\alpha$ closely matches the experimental values; see Fig. 9(b)). Comparisons of these isosurface shapes with those of the crystalline reference phases reveal similar shapes and characteristics: compare Figs. 10(a-b) with 8(a-b). This supports our assumption that localized electronic screening of core-ionized Al atoms by nearest-neighbour O and OH ligands in the studied amorphous alumina polymorphs is very similar to those in the crystalline oxide and hydroxide reference phases.

Further validation is provided in Fig. 10(c), which shows the distributions of the Bader charge, q_{B} , for Al and H atoms, as well as for O atoms with and without H neighboring atoms in sapphire, bayerite, and in H-rich and H-poor amorphous polymorphs (i.e. for H/Al=1 and H/Al=0.013, respectively). Al cations exhibit relatively narrow distributions of q_{B} compared to O, being extremely narrow for the crystalline references. The amorphous polymorphs display slightly broader q_{B} distributions for Al. This indicates that the valence charge density of Al is only very slightly affected by hydrogen bonding to nearest-neighbour O ligands. Accordingly, the mean q_{B} values for Al are similar for all studied structures, ranging approximately from 2.46e to 2.47e in agreement with Ref. [118]. Particularly interesting are the q_{B} distributions for O ligands with and without H neighbors: see central column of Fig. 10(c). It shows that O atoms without neighboring H have a mean q_{B} similar to that of sapphire, while O atoms with neighboring H have a mean q_{B} similar to that of bayerite. This nicely demonstrates why the adopted model and assumptions are so successful in predicting $\Delta\alpha_{\text{Al}}$ as a simple function of the fraction of hydroxyl ligands in

amorphous polymorphs. The corresponding mean values of q_B for H atoms are also similar for both amorphous polymorphs and bayerite. The narrow q_B distributions of H for bayerite and the Al-poor amorphous polymorphs ($H/Al=0.013$) originate from the fact that all H atoms have identical local chemical environments in the two different structures: i.e. long-range ordered $[Al(OH)_6]$ NNCS in bayerite and isolated $[Al(O)_{n-1}(OH)]$ NNCS (with $n = 4, 5$ or 6) in the Al-poor amorphous polymorph. With increasing H content, $[Al(O)_{n-m}(OH)_m]$ NNCS with more than one OH ligand (i.e. for $n = 4, 5$, or 6 with $1 < m < n$) will be very common. Indeed, as evidenced by the analysis of the average O/OH ligand fractions for 4-fold, 5-fold and 6-fold NNCS in the amorphous polymorphs in Appendix D, the $[Al(O)_{n-m}(OH)_m]$ NNCS in the H-rich amorphous polymorph (for $H/Al=1$) can have up to $m = 4$ hydroxyl ligands, whereas the H-poor amorphous polymorphs (for $H/Al=0.02$) either have zero or a single OH ligand. The presence of multiple hydroxyl ligands in a given $[Al(O)_{n-m}(OH)_m]$ NNCS will result in a distribution of local distortions with respect to the $[Al(O)_n]$ NNCS in anhydrous $am-Al_2O_3$, resulting in broader isosurfaces for the valence electrons of O and H (but much less for those of Al).

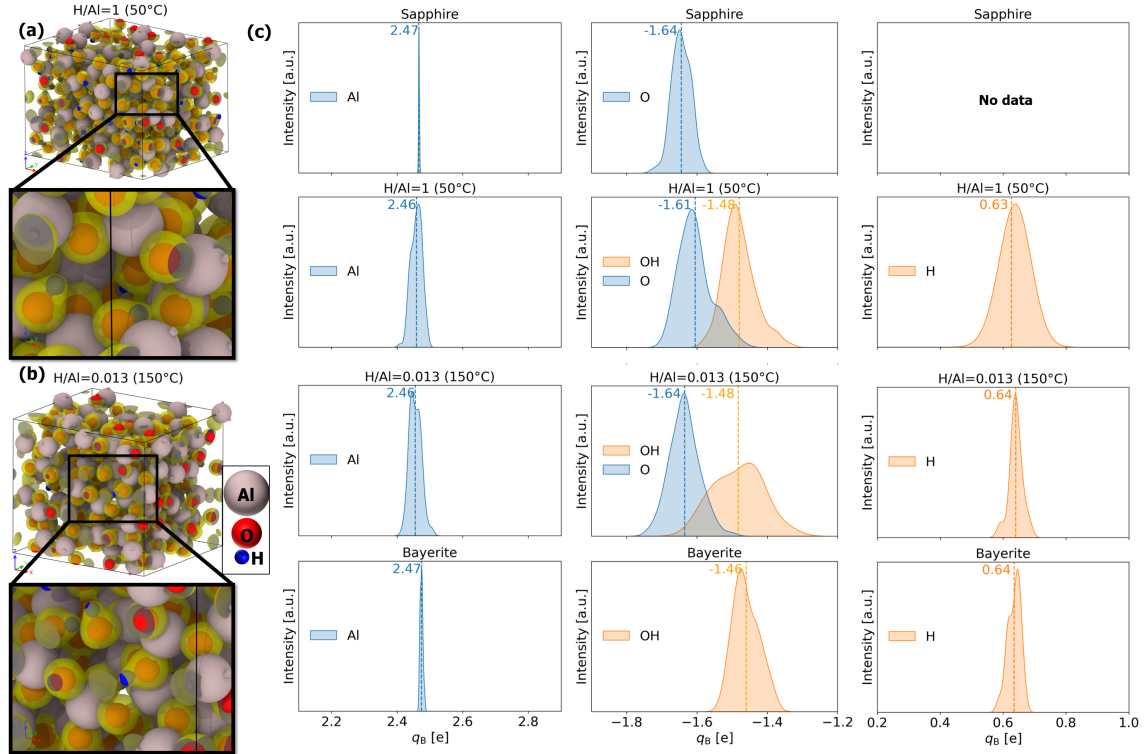


Figure 10: Reconstructed isosurfaces of oxygen valence electrons for (a) an Al-rich ($H/Al=1$) and (b) an Al-poor ($H/Al=0.013$) amorphous polymorph, showcasing the spatial distribution and density. (c) Kernel density estimates of Bader charges, q_B , for aluminum, oxygen, hydroxyl, and hydrogen atoms, organized into three respective columns. Each row represents a different sample: the first row pertains to Sapphire, the second to the Al-rich amorphous polymorph with $H/Al=1$, the third to the Al-poor amorphous polymorph with $H/Al=0.013$, and the final row to Bayerite. The mean values of the Bader charge distributions are indicated by the dashed lines.

As reflected in Figs. 7(a-c), the amorphous polymorphs exhibit similar trends in their structural parameters as a function of H content, except for the amorphous polymorph with the lowest H content, corresponding to the highest ALD temperature of 200 °C. In this regard, it is emphasized that this $am-Al_2O_3$ ALD film is superimposed to thermal annealing at 200 °C during its 4 hrs deposition run [34]. As mentioned above, this highest ALD growth (and annealing) temperature exceeds the onset temperature for the crystallization of $am-Al_2O_3$ in the range of 180 - 200 °C [112, 72]. This implies that simultaneous thermal annealing of the growing ALD film at 200 °C is accompanied by slow but gradual crystallization [112, 72], which should be more pronounced for the initially deposited, interface-adjacent regions of the $am-Al_2O_3$ film. This crystallization will be accompanied by a gradual release of hydroxyl ligands and a modification of the isolated $[Al(O)_{n-1}(OH)]$ building blocks in the $am-Al_2O_3$ film [82]. Indeed, the n , D , and r values all sharply increase towards those for sapphire for an increase of the ALD deposition temperature from 150 °C to 200 °C. Consequently, our presumption that all H impurity atoms are bonded to O

in the form of hydroxyl ligands may be violated for the ALD film grown at 200 °C. This rationalizes the underestimate of $\Delta\alpha_{\text{Al},s}$ with respect to $\Delta\alpha_{\text{Al}}$ for $T = 200$ °C in Fig. 9(b).

This hypothesis is investigated in more detail in Fig. 11, which shows the distributions of the Bader charge, q_B , for Al and H atoms, as well as for O atoms with and without H neighboring atoms, below and above the onset of the crystallization temperature range (i.e. for H/Al=0.2 and H/Al=0.013 pertaining to an ALD deposition temperature of 120 °C and 200 °C, respectively). Two distinct peaks for the OH ligands are visible for $T = 200$ °C, one having a mean q_B similar to bayerite and the amorphous polymorph for $T = 120$ °C (H/Al=0.2). The other peak has a significantly lower mean, shifting the overall mean of q_B towards -1.51. This broadening by splitting-up of the q_B distribution for O may be tentatively contributed to the reduction of free volume and the development of long-range between the interconnected $[\text{AlO}_n]$ polyhedral building blocks upon crystallization [112, 72], as accompanied by a gradual transformation of isolated hydroxyl species into O ligands and interstitial protons and/or O–H··O bridging configurations [116, 115, 77].³ Consequently, the mixing rule used to fit ζ values for calculating $\Delta\alpha$ becomes invalid. The considerable underestimation of $\Delta\alpha_{\text{Al},s}$ with respect to $\Delta\alpha_{\text{Al}}$ for $T = 200$ °C in Fig. 9(b) would imply an underestimation of the ligand polarizability of core-ionized Al ions for the amorphous polymorph at 200 °C.

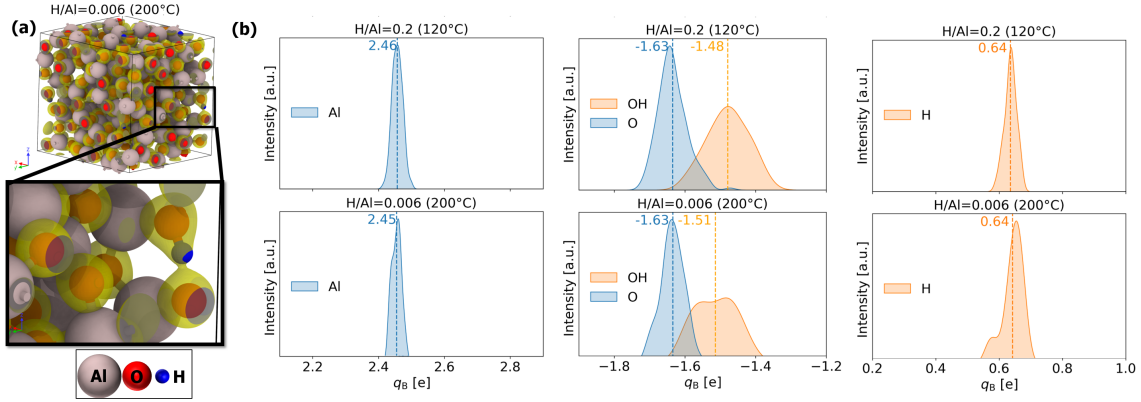


Figure 11: Panels (a) depict the isosurfaces of oxygen valence electrons for H/Al=0.006, showcasing the spatial distribution and density. Panel (b) presents kernel density estimates of Bader charges for Al, O, OH, and H atoms, organized into three respective columns. Each row represents a different sample: the first row displays the H/Al=0.2 sample, the second shows the H/Al=0.006. The mean values of the distributions are indicated and given as dashed lines.

3.2. Model predictions using the complete electrostatic model

The Bayesian optimization process for the complete model is much more computationally intensive than for the simplified model, as the distribution for $\Delta\alpha_{\text{Al},c}$ must be calculated for every Al atom and frame of the MD trajectory, each time a new set of polarizabilities is tested. Consequently, fewer optimization steps (34) were performed, while setting the lower and upper limits in a narrower range, as the expected ζ values lie between 1 and 3. Fig. 12(a) displays the results of Bayesian optimization, with the maximum of the objective function being achieved with $\zeta_{\text{OH},c} = 1.749 \text{ \AA}^3$ and $\zeta_{\text{O},c} = 2.189 \text{ \AA}^3$, which are only about 0.2% and 1.7% smaller than the corresponding values derived using the simplified model. The overall value of the objective function given by Eq. (13) is higher than that of the simplified model, indicating that the full model provides incrementally better agreement with the experimental results. This improvement is visualized in Fig. 12(b), where $\Delta\alpha_{\text{Al},c}$ and $\Delta\alpha_{\text{Al},s}$ are compared with the experimental data.

³Notably, a similar broadening by splitting-up of the q_B distribution appears to evolve in the amorphous polymorph for $T = 150$ °C (H/Al=0.013; see Fig. 10(b)), albeit less pronounced as for $T = 200$ °C.

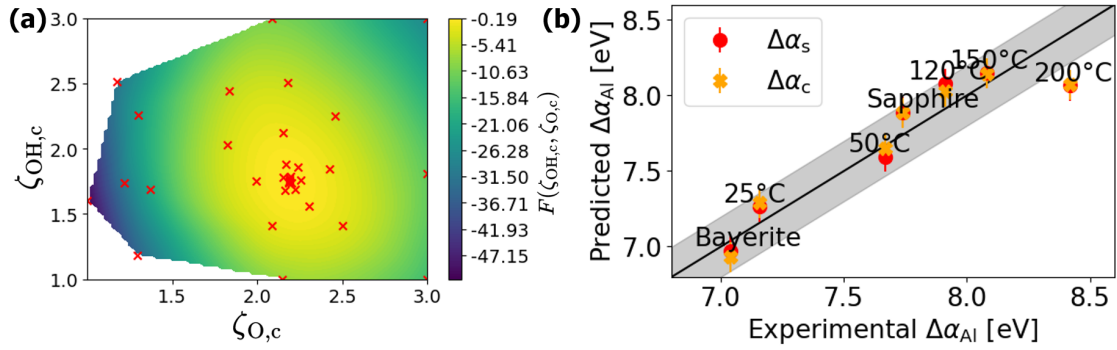


Figure 12: Visualization of the Bayesian optimization process: (a) Application to the full electrostatic model, involving 34 optimization steps. (b) The shift of the Al Auger Parameter as calculated using the simple electrostatic model ($\Delta\alpha_{\text{Al},s}$) and the full electrostatic model ($\Delta\alpha_{\text{Al},c}$) versus the experimentally determined value, $\Delta\alpha_{\text{Al}}$. Points lying on the diagonal black line represent perfect agreement with experimental data. The surrounding gray area delineates the empirical experimental error of ± 0.2 eV.

To illustrate the strengths of the full model, a detailed analysis of the atomistic simulation data is provided below. Evidently, the distribution of the structural parameters n , D , r and f_{OH} over each individual Al atom in a given alumina structure is different for each simulated structure and also varies with (simulation) time. This distribution in local structure and composition (as superimposed by thermal fluctuations) results in a characteristic distribution of ligand polarizabilities for each simulated structure, which translates into a specific distribution of final-state relaxation energies, ΔR^{ea} , as shown in Fig. 13 for bayerite, sapphire and the *am*- Al_2O_3 polymorphs with various H/Al-ratios for $T = 25$ °C, $T = 50$ °C and $T = 120$ °C (with final thermal equilibration T_{E} at 10 K, 100 and 300 K).

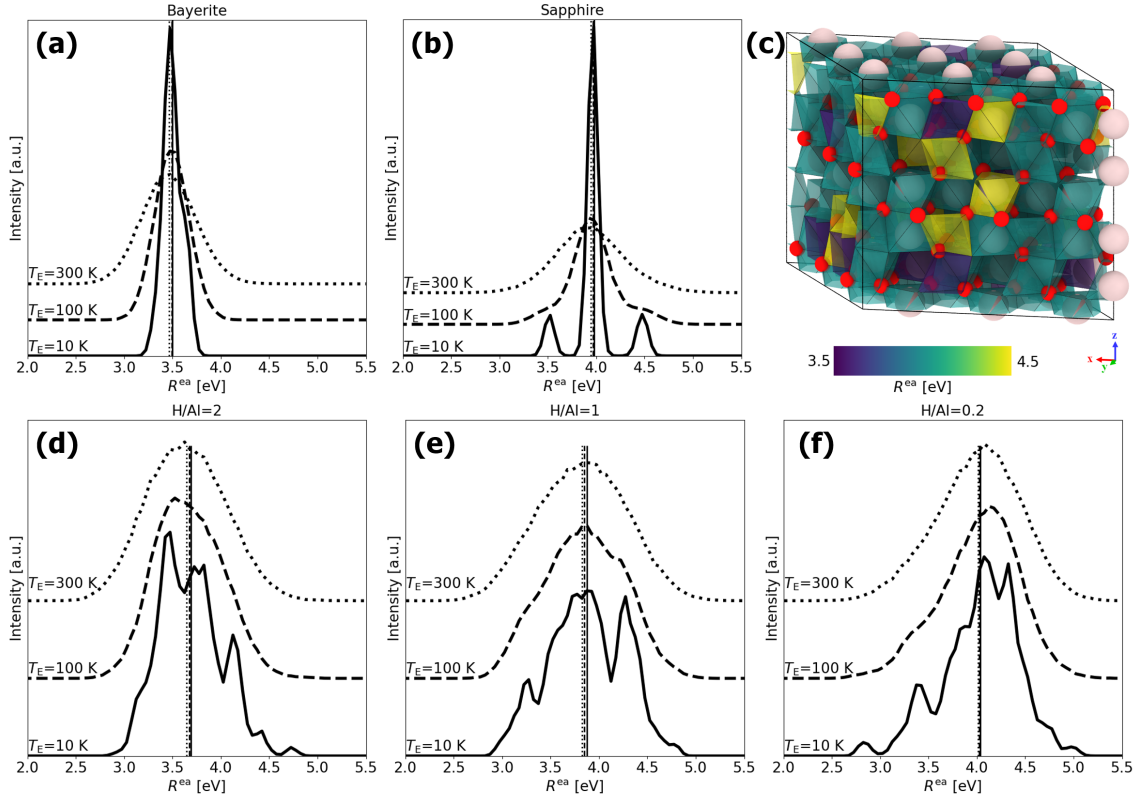


Figure 13: Distributions of the extra atomic relaxation energy, R^{ea} , as derived from the full model for (a) bayerite, (b) sapphire, (d) the $am\text{-Al}_2\text{O}_3$ polymorph with $\text{H}/\text{Al}=2$ at $T = 25$ °C, (e) the $am\text{-Al}_2\text{O}_3$ polymorph with $\text{H}/\text{Al}=1$ at $T = 50$ °C, and (f) the $am\text{-Al}_2\text{O}_3$ polymorph with $\text{H}/\text{Al}=0.2$ at $T = 120$ °C. The distributions are shown for three different final thermal equilibration temperatures T_E with the solid, dashed, and dotted lines referring to $T_E = 10$ K, $T_E = 100$ K, and $T_E = 300$ K, respectively. The corresponding vertical lines indicate the mean value of each distribution. (c) Illustration of the building blocks corresponding to the different peaks in the R^{ea} distribution plot for sapphire at $T = 10$ K in (b), as visualized by colored coordination polyhedra.

As expected, the ΔR^{ea} distributions are symmetric and much narrower and smoother for the crystalline reference phases sapphire and bayerite (as compared to the $am\text{-Al}_2\text{O}_3$ polymorphs), owing to their defined lattice periodicity and limited structural diversity (i.e. all Al cations in 6-fold coordination). The broadening of the distributions with an increasing equilibration temperature for sapphire and bayerite can be attributed to increasing thermal fluctuations. Interestingly, the ΔR^{ea} distribution for sapphire reveals a symmetric fine structure at cryogenic temperatures of $T = 10$ K, which originates from two specific Al-O bond lengths in sapphire [119] in three distinct types of building blocks, as illustrated in Fig. 13(c). Provided that the experimental resolution suffices, such subtle differences might be resolved by XPS analysis of sapphire at cryogenic temperatures, which motivates a the broader application of cryo-XPS/HAXPES for chemical state analysis.

The fine structures underlying the peak asymmetries in the ΔR^{ea} distributions of the amorphous polymorphs (see Figs. 13(d-f)) become visible by removing broadening due to thermal fluctuations. It follows that, in contrast to the crystalline references, the ΔR^{ea} distributions for the amorphous polymorphs do not narrow with decreasing equilibration temperature; this indicates that the observed spread in ΔR^{ea} originates from structural diversity rather than from thermal fluctuations. At $T = 100$ K, a skewness of the ΔR^{ea} distributions becomes apparent, which are in opposite directions with respect to the mean ΔR^{ea} value for $\text{H}/\text{Al}=2$ and $\text{H}/\text{Al}=1$ (with $\text{H}/\text{Al}=1$ lying in between). It is very challenging to identify individual contributions of the specific structural building blocks to these fine structures and the resulting skewness of the ΔR^{ea} distributions, because of the co-existence of distorted 4-fold, 5-fold, and 6-fold $[\text{Al}(\text{O})_{n-m}(\text{OH})_m]$ NNCS with variable O/OH-ligand fractions. This is illustrated in the Appendix Appendix D by dissecting each amorphous oxide polymorph (as equilibrated at 10 K) in 2D histograms of their 4-fold, 5-fold, and 6-fold $[\text{Al}(\text{O})_{n-m}(\text{OH})_m]$ NNCS with resolved average fractions of O and OH ligands for each of these building blocks. This building block analysis confirms previous statements (cf. Section 3.1) that the pertinent $[\text{Al}(\text{O})_{n-m}(\text{OH})_m]$ NNCS are those with $n = 4, 5, 6$, with $n = 5$ being the largest group in each distribution

(especially for high H/Al-ratios), in accordance with literature [120, 121, 122, 123, 124, 125, 126].

As follows from Fig. D3, each specific $[\text{Al}(\text{O})_{n-m}(\text{OH})_m]$ NNCS results in a spread of the individual R^{ea} ligand values. This is not surprising, as even for a highly ordered crystalline phase such as sapphire (with a single ligand type and a single coordination), three distinct R^{ea} ligand values can be found (see above). Nevertheless, a general statement can be made that $[\text{Al}(\text{O})_{n-m}(\text{OH})_m]$ NNCS with a large number of ligands and/or a higher average O/OH ligand fraction dominate the R^{ea} contributions on the upper side of the mean value ΔR^{ea} value (since $\zeta_{\text{O}} > \zeta_{\text{OH}}$ and the screening efficiency increases with increasing coordination number, n ; see Section 3.1). The structural building block analysis in Fig. D3 further indicates that NNCS with the same total number of ligands (with the same n value) tend to contribute to the same side of the ΔR^{ea} distribution, independent of the ligand type. This is illustrated in Fig. 14, which classifies the 4-fold, 5-fold and 6-fold contributions to ΔR^{ea} for the amorphous polymorphs with H/Al=2, H/Al=1 and H/Al=0.2 at 100 K. Clearly, the R^{ea} distributions from $n = 5$ and $n = 6$ present similar mean and mode values (e.g. around 3.5 eV) for a high H content (H/Al=2) with the corresponding distribution for $n = 4$ being shifted by more than 0.5 eV (to 4.1 eV). This division between 5/6-fold and 4-fold NNCS contributions to ΔR^{ea} becomes less pronounced with decreasing H content due to a gradual broadening of all distributions (especially from 5- and 6-fold NNCS) towards higher R^{ea} values (since $\zeta_{\text{O}} > \zeta_{\text{OH}}$). These findings suggest that the measured asymmetry of the core-level photoelectron line of the respective cation (*here*: Al 2p; as preferably measured by cryo-XPS to reduce thermal noise) might actually provide an alternative method for quantifying the hydrogen content and related structural changes of the NNCS in H-containing amorphous oxides. The corresponding *absolute* peak shift might be much more difficult to interpret due to the superposition of initial- and final-state effects (see Introduction). In this regard, it should be emphasized that asymmetric peaks in XPS may also arise from satellite structures, excitation of vibrational modes, multi-electron excitations, and electron-hole pair creation in metallic valence bands [127].

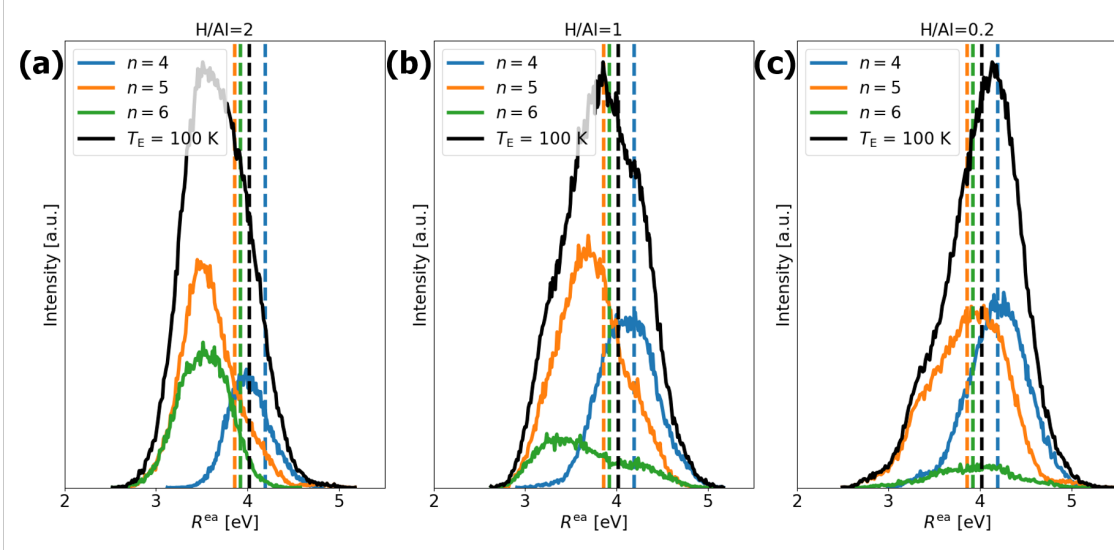


Figure 14: Analysis of the NNCS contributions to R^{ea} (for thermal equilibration at $T = 100$ K), as based on the nearest-neighbor ligands count (i.e. $n = 4, 5, 6$) for amorphous polymorphs with (a) H/Al=2, (b) H/Al=1 and (c) H/Al=0.2. Dashed lines highlight the mean value of each individual distribution.

In summary, the combination of atomistic simulations with experimental characterization and electrostatic modeling, as presented in this work, opens new avenues for investigating the local chemical bonding states and structure of crystalline and amorphous materials, whose interaction with X-rays is dominated by R^{ea} . Possible materials are Al, Si, and Mg oxides, zeolites, and other materials where the Auger parameter of cations is far from the metallic state and driven by extra-atomic relaxation energy, see Ref. [110]. We demonstrate that the nature of H impurities in such compounds can be revealed by comparing the experimental Auger parameter shifts with those predicted from simple electrostatic theory by assuming that a dominant fraction of incorporated hydrogen atoms participates in OH hydroxyl bonds. Any deviation between experiment and theory beyond the experimental error indicates the co-existence of different H bonding states, such as interstitial H protons and/or O–H···O bridging configurations. Such fundamental knowledge provided by careful analysis of experimentally measured Auger shifts might contribute to advance the design of hydrogen barrier films, hydrogen separation membranes, hydrogen storage materials and fuel cells, for a diverse range of technologies.

4. Conclusion

In this study, we have explored several key aspects of the Auger parameter shifts invoked by the incorporation of hydrogen in amorphous and crystalline oxides, in particular, for amorphous alumina oxide films grown by atomic layer deposition. Initial efforts to simulate structures of the ALD amorphous polymorphs with different H contents and densities, which closely resemble those observed in the experiment, showed that the traditional melt quenching procedure is not applicable for generating representative structures of H-containing amorphous oxides. Therefore, we adopted a novel approach for simulating amorphous H-containing amorphous oxide structures by annealing artificially constructed, highly defective crystalline hydroxide structures with experimental H/Al-ratios and densities at their respective ALD growth temperatures, using a universal machine learning interatomic potential (while maintaining nominal charge neutrality). This resulted in excellent representatives of the real experimental structures, evidencing that the novel approach is much more effective than the conventional simulation approach in simulating amorphous oxide structures with variable H contents. The striking agreement between the structures and densities of the simulated and experimental amorphous oxides also indicates a high reliability of the universal machine learning interatomic potential used.

Next, it was demonstrated that the Auger parameter shifts of the Al cations in Al-O-based compounds are governed by the final-state extra-atomic relaxation energy, which validates the use of simple electrostatic models to interpret these shifts quantitatively. The average polarizabilities of O and OH ligands of $\zeta_{\text{OH}} = 1.753 \text{ \AA}^3$ and $\zeta_{\text{O}} = 2.227 \text{ \AA}^3$, respectively, were derived from the simulated amorphous structures (as well as from sapphire and bayerite crystalline reference phases) by application of a simplified electrostatic model by Moretti under the presumption that all H atoms bond to O nearest-neighbouring ligands of the Al cations in the form of OH hydroxyl ligands. This resulted in excellent agreement between measured and predicted Auger parameter shifts for Al as a function of the H-content, thus validating the fact that effective ligand polarizability can be derived through the mixing rule from the fraction of OH ligands. On the basis of these findings, a simple equation is provided that relates the Auger parameter shift to the average coordination, bond length, and ligand polarizability of the compound of interest, which is applicable not only for crystalline compounds but also for amorphous compounds with mixed ligand types. Only at elevated growth temperatures of $T > 180 \text{ }^\circ\text{C}$, the onset of crystallization induces a gradual transformation of isolated hydroxyl species into O ligands and interstitial (more mobile) protons and/or O-H \cdots O bridging configurations, resulting in an underestimation of the average ligand polarizability (and the corresponding Al Auger parameter shift).

The application of a full electrostatic description of the ligand polarizability by Moretti resulted in only slightly higher ligand polarizabilities of $\zeta_{\text{OH},c} = 1.749 \text{ \AA}^3$ and $\zeta_{\text{O},c} = 2.189 \text{ \AA}^3$ (as compared to those determined with the simple electrostatic model). The application of the full electrostatic model to the simulated amorphous structures discloses the effect of thermal vibrations on the distribution of the extra-atomic relaxation energies of the O and OH ligands in the amorphous alumina polymorphs. It is thus argued that cryogenic XPS might offer new insights into the local chemical bonding states and structure of crystalline and amorphous oxides by reducing thermal noise, thereby providing a more universal picture of the material’s intrinsic properties. The distribution of relaxation energies in the amorphous alumina polymorphs exhibit a positive shift of its mean value (and a change in skewness of its asymmetric peak shape) with decreasing H content, which can be attributed to a decrease in the average ligand coordination number of Al and an accompanied increase of the average fraction of O ligands in randomly interconnected 4-fold, 5-fold and 6-fold $[\text{Al}(\text{O})_{n-m}(\text{OH})_m]$ nearest-neighbour coordination spheres (NNCS; with $n = 4, 5, 6$ and $0 < m < n$).

In summary, our work provides a comprehensive understanding of Auger parameter shifts and hydrogen-induced local chemical bonding states in amorphous alumina films, which pave the way for further research and development on amorphous, crystalline, and hydrogen-doped materials, for a wide range of materials technologies.

5. Acknowledgments

This research was supported by NCCR MARVEL, a National Centre of Competence in Research, funded by the Swiss National Science Foundation (grant number 205602). We acknowledge financial support from the Swiss National Science Foundation (R’Equip program, Proposal No. 206021.182987).

6. Data availability statement

Data supporting the findings of this study are openly available at the following URL/DOI: <https://doi.org/10.24435/materialscloud:9v-61> [78].

Appendix A. Interatomic Potential Justification

We begin our tests with the comparison of equilibrium structures of sapphire and bayerite. The initial configurations have been taken from the Materials Project (next-gen.materialsproject.org/materials/mp-1143, next-gen.materialsproject.org/materials/mp-560572). These configurations underwent energy minimization with PFP in LAMMPS (energy tolerance 10^{-4} eV) and force tolerance (10^{-6} eV/Å) with box relaxation to zero values of the six components of the pressure tensor. In Table A1, we directly compare the unit cell vectors and densities of our simulated structures with the values obtained from DFT calculations and experimental data. PFP is designed to predict the energies and forces derived from DFT computations with Projector augmented wave (PAW) pseudopotentials Perdew-Burke-Ernzerhof (PBE) functional. Thus, it demonstrates quite a good accuracy when compared to DFT results, but it does not perform well against experimental data.

Despite the broad applicability of DFT across various material systems, it encounters limitations in accurately capturing certain phenomena, notably those involving dispersion forces (Van der Waals forces). These forces play a significant role in simulations in which dipole interactions, stemming from electronic state excitations, are critical to capture the properties of oxides, hydroxides, and especially layered materials [128, 129, 130, 131]. The primary focus of DFT on the electronic ground state presents challenges in directly addressing dispersion forces. To mitigate these limitations, the DFT-D3 method emerges as a prevalent solution, effectively accounting for the dispersion force contributions while combined with the PBE pseudopotential [104, 132]. This approach involves the explicit computation of the dispersion force energy (D3 correction) and its subsequent addition to the DFT-derived energy [133]. This synergy allows for a more nuanced simulation of material behavior, bridging the gap between theoretical accuracy and computational efficiency.

Leveraging the torch-dftd framework [134], the PFP model incorporates the D3 correction to improve its accuracy in simulating material properties with a marginal increase in computational time. As shown in Table A1, PFP+D3 matches better experimental densities, cell vectors a, b, c , and cell angles α, β and γ as compared to PFP. This evidence strongly advocates for the utilization of PFP+D3 in current modeling efforts, especially in contexts where accurate reproduction of experimental results is critical.

Table A1: Comparison of different properties between crystalline reference structures of bayerite and sapphire, juxtaposed with experimental and ab initio data. The computational models include structures obtained through PFP + D3, PFP, and DFT modeling. These computational results correspond to structures stabilized at $T = 0$ K. In contrast, the experimental data were acquired at 25°C, offering a relevant comparison across different conditions and methodologies.

Property	Bayerite				Sapphire			
	PFP + D3	PFP	DFT	Exp. (25°C)	PFP + D3	PFP	DFT	Exp.
ρ [g/cm ³]	2.50	2.36	2.39 [135]	2.50[34, 61]	3.90	3.82	3.87 [136]	3.9-3.98 [34, 119]
a [Å]	5.08	5.15	5.15 [135]	5.06 [61]	4.80	4.82	4.81 [136]	4.76 [119]
b [Å]	8.73	8.84	8.92 [135]	8.68 [61]	4.80	4.82	4.81 [136]	4.76 [119]
c [Å]	9.34	9.63	9.42 [135]	9.42 [61]	13.08	13.17	13.12 [136]	13.00 [119]
α [°]	90.00	90.00	90.00 [135]	90.00 [61]	90.00	90.00	90.00 [136]	90.02 [119]
β [°]	90.41	90.26	90.49 [135]	90.49 [61]	90.00	90.00	90.00 [136]	89.98 [119]
γ [°]	90.00	90.00	90.00 [135]	90.00 [61]	120.00	120.00	120.00 [136]	120.01 [119]

The structure of a given amorphous oxide (e.g. its density) strongly depends on the synthesis method (both in experiments and atomistic modeling), which renders it unsuitable for benchmarking the model. Therefore, our analysis shifts to the disordered structure of liquid alumina, as modeled using both PFP and PFP+D3, against experimental data derived from neutron scattering [137] and X-ray scattering [81] experiments. The comparative results are illustrated in Fig. A1, which presents an overlay of the radial distribution functions $g(r)$ for stoichiometric liquid alumina. As shown in Fig. A1, the comparison between the liquid alumina structures modeled by PFP and those by PFP+D3 reveals negligible differences, affirming the applicability of the PFP+D3 potential for studying alumina and for subsequent analyses within this

study. This observation underscores the potential’s capability to capture the essential characteristics of liquid alumina, without significant alterations attributed to the inclusion of D3 corrections.

Noteworthy, the mean Al-O bond length across all methodologies hovers around $r \approx 1.76 \text{ \AA}$, indicating a consistent representation of this fundamental structural parameter. However, discrepancies arise when considering the position of the second peak at $\approx 2.9 \text{ \AA}$, which corresponds to both O-O and Al-Al distances [84]. Typically, neutron scattering provides more accurate information for lighter elements like oxygen, whereas X-ray scattering is more effective for electron-rich atoms such as aluminum. Consequently, the overlap in the second peak leads to a broader experimental peak, whereas atomistic simulations display a more defined second peak position that does not fully match either experimental measurement. This misalignment suggests potential limitations in the experimental resolution or the simulation model’s ability to concurrently capture the dynamics of both light and heavy elements with equal precision.

The structural composition of liquid alumina, as evidenced through neutron scattering [137, 84], NMR [138], and X-ray studies [81], represents a macroscopic averaging of various local atomic arrangements. These arrangements, rather than being static, are part of a dynamic equilibrium, contributing to the complexity and connectivity observed within the liquid alumina structure. However, it is essential to recognize that the coordination numbers derived from neutron scattering data, which suggest a lower density for the high-temperature liquid compared to sapphire [84], reflect the alterations in aluminum and oxygen coordination in response to temperature variations.

This diverse spectrum of experimental evidence highlights the challenge of pinpointing a definitive structural model for liquid alumina. The dynamic nature of atomic coordination and the variability across different experimental methods suggest that the true structure likely embodies aspects of each observed configuration. In this context, the PFP potential emerges as a promising tool for bridging these experimental observations, offering a comprehensive model that may well align with the multifaceted reality of liquid alumina’s structure.

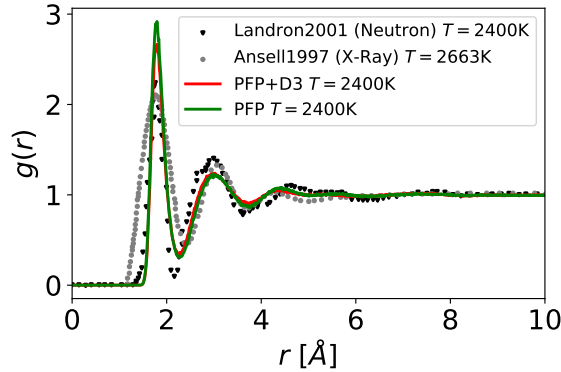


Figure A1: Total radial distribution functions, $g(r)$, for liquid Al_2O_3 at a temperature of $T = 2400 \text{ K}$. The presented data are compared against experimental benchmarks derived from neutron scattering and x-ray experiments conducted by Landron *et al.* [137], and Ansell *et al.* [81], respectively.

Appendix B. Atomistic Simulation Cells

Table B2: Details of the simulations cells used in the atomistic simulations including type of phase, ALD growth temperature, H/Al ratio, numbers of Al, O, H atoms, and cell parameters a , b , c , α , β , γ .

Sample	H/Al ratio	# Al	# O	# H	a [Å]	b [Å]	c [Å]	α [°]	β [°]	γ [°]
Sapphire	0.00	108	162	0	14.39	14.39	13.08	90.00	90.00	120.00
Bayerite	3.00	128	384	384	20.33	17.46	18.68	90.00	90.41	90.00
Amorphous (25°C)	2.00	128	320	256	19.97	16.74	18.60	90.18	91.03	90.38
Amorphous (50°C)	1.00	128	256	128	19.14	17.04	14.49	90.29	90.43	88.13
Amorphous (120°C)	0.20	128	205	26	16.89	14.45	15.53	89.21	89.78	88.55
Amorphous (150°C)	0.13	128	200	16	16.74	14.65	15.05	92.33	88.29	88.46
Amorphous (200°C)	0.06	128	196	8	16.58	14.00	15.26	89.90	92.28	88.93

Appendix C. Geometrical factor, D , and Al-O bond length, r , in relation to coordination number, n

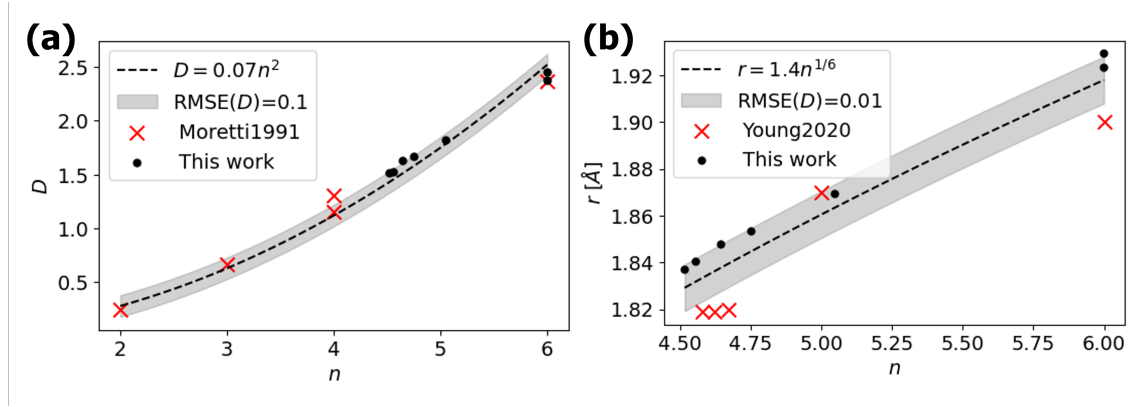


Figure C2: (a) Dependency of the geometrical factor, D , on the coordination number, n . The data is fitted with a power law, $D = D_0n^2$, using the least squares error method, where $D_0 = 0.07$. Structures used in this study are shown in black, and those from [90] are shown in red. The grey area around the fitted curve represents the root mean square error (RMSE) of 0.1. (b) Dependency of the bond length, r , on the coordination number, n . The data is fitted with a power law, $r = r_0n^{1/6}$, using the least squares error method, where $r_0 = 1.4$. Structures used in this study are shown in black, and those from [114] are shown in red. The grey area around the fitted curve represents the RMSE of 0.01.

Appendix D. Chemical environment of Al

In the following, we investigate which local chemical environments around the Al atoms contribute most significantly to the splitting of the R^{ea} peaks at $T_{\text{R}} = 10$ K, and whether it is possible to directly associate individual structural building blocks of the amorphous alumina polymorphs to specific features in the fine-structure of the R^{ea} distribution resolved for an equilibration temperature of $T_{\text{E}} = 10$ K (i.e. by removal thermal noise). For this, the individual Al atoms in the structures were categorized based on their number of O (n_{O}) and OH (n_{OH}) ligands, adopting a cutoff distance of 1.2 \AA following the same procedure used for determining f_{OH} and f_{O} in Section 3.1. Considering that each Al atom can be coordinated by up to six ligands, there are theoretically $7 \times 7 = 49$ different groups based on the n_{O} and n_{OH} values. This grouping was performed across the entire trajectory of the $T_{\text{E}} = 10$ K equilibrated structures, as the peak splitting is particularly evident at this low temperature. The count of groups — and hence, the intensity in % contributing to the overall R^{ea} per sample — is represented by the height of bins in a 3D histogram. In this histogram, the x and y positions correspond to n_{O} and n_{OH} for each group, and the bin color reflects the average R^{ea} for that group of Al atoms. This data is depicted for three different samples (H/Al ratios of 2, 1, and 0.2) in Fig. D3(a-c), respectively.

Fig. D3(a) illustrates that, for H/Al=2 (corresponding to the highest H content), the primary contributing group is Al with $n_{\text{O}} = 0$, $n_{\text{OH}} = 6$. The intensity of groups decreases diagonally in the n_{O} , n_{OH} array, with a notably higher peak for the $n_{\text{O}} = 3$, $n_{\text{OH}} = 1$ group, suggesting potential tetrahedral coordination of Al with three OH and one O ligand. For H/Al=1, as depicted in Fig. D3(b), the central area of the n_{O} , n_{OH} array contributes to the main peaks, with comparable contributions from groups indicative of four or five coordinated Al atoms, which generally are the principal building blocks of amorphous alumina: $n_{\text{O}} = 2$, $n_{\text{OH}} = 3$; $n_{\text{O}} = 3$, $n_{\text{OH}} = 2$; $n_{\text{O}} = 3$, $n_{\text{OH}} = 1$; $n_{\text{O}} = 4$, $n_{\text{OH}} = 1$; and $n_{\text{O}} = 4$, $n_{\text{OH}} = 0$. Finally, the H-poor amorphous polymorph with H/Al=0.2 in Fig. D3(c) is characterized by groups lacking OH ligands, specifically $n_{\text{O}} = 5$, $n_{\text{OH}} = 0$, and $n_{\text{O}} = 4$, $n_{\text{OH}} = 0$, reflecting the characteristic four and five-fold coordination of Al in amorphous alumina.

Specific R^{ea} contributions of selected coordination variants pertaining to Figs. D3(a-c), along with their R^{ea} distribution are displayed in Figs. D3(d-f) for the three representative alumina polymorphs (H/Al=2, 1, 0.2). For H/Al=2 (Fig. D3(d)), the splitting into three distinct subpeaks of the full $T = 10$ K R^{ea} distribution can each be correlated with specific n_{O} , n_{OH} groups. The first subpeak, featuring the lowest R^{ea} , predominantly originates from the $n_{\text{O}} = 0$, $n_{\text{OH}} = 6$ and $n_{\text{O}} = 1$, $n_{\text{OH}} = 4$ groups, while the third subpeak, represents higher R^{ea} values which are largely composed of the $n_{\text{O}} = 3$, $n_{\text{OH}} = 1$ group. The central peak does not distinctly correspond to specific groups but appears to be a composite of several

contributions. For the H/Al=1 sample (Fig. D3(e)), three major subpeaks can again be discerned. The lowest energy peak primarily originates from the group with the highest OH content, specifically $n_{\text{O}} = 2$, $n_{\text{OH}} = 3$. The middle subpeak, similar as for H/Al=2, consists of mixed contributions from several groups. The highest energy subpeaks are predominantly composed of the $n_{\text{O}} = 4$, $n_{\text{OH}} = 1$ and $n_{\text{O}} = 4$, $n_{\text{OH}} = 0$ groups, that have the most O ligands. For H/Al=0.2, (Fig. D3(f)), a minor peak at low energy primarily consists of the $n_{\text{O}} = 4$, $n_{\text{OH}} = 1$ group, the principal group containing OH ligands. The remainder of the distribution largely emanates from the $n_{\text{O}} = 5$, $n_{\text{OH}} = 0$ and $n_{\text{O}} = 4$, $n_{\text{OH}} = 0$ groups. Overall, these distributions reveal that groups with a greater number of ligands exhibit slightly reduced R^{ea} . Furthermore, groups predominantly bonded with OH ligands tend to shift R^{ea} towards lower energies, whereas Al groups mainly coordinated with O ligands tend to shift R^{ea} towards higher energies, which should be attributed to the different ligand polarizabilities of O and OH.

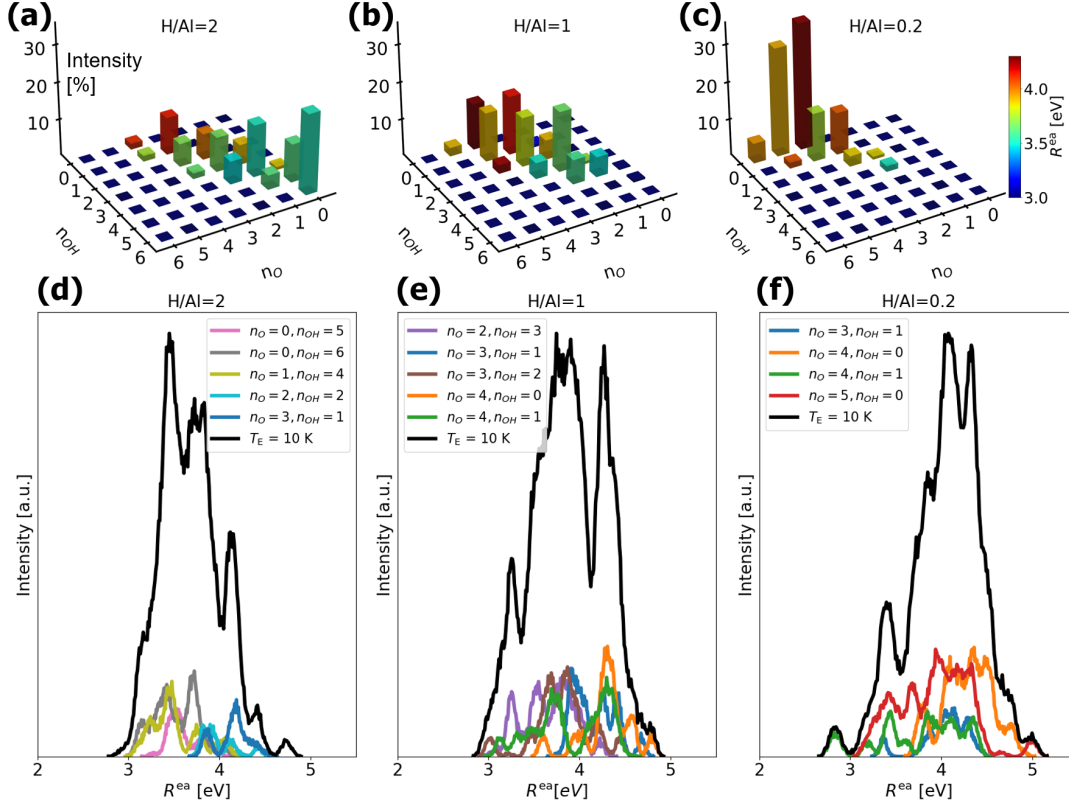


Figure D3: Exploration of the local chemical environments around Al atoms and their significant contributions to the splitting of the R^{ea} peaks. This analysis aims to link the individual structural building blocks of the amorphous alumina polymorphs with specific peak characteristics. Al atoms were classified according to their number of oxygen (O) (n_{O}) and hydroxyl (OH) (n_{OH}) ligands, utilizing a cutoff distance of 1.2 Å. This study spans the entire trajectory of amorphous polymorphs maintained at $T_{\text{E}} = 10$ K, as depicted in 3D histograms for three representative polymorphs with differing H/Al ratios of 2, 1 and 0.2 (corresponding to ALD temperatures of 25°C, 50°C, and 120°C, respectively), as shown in (a), (b), and (c), respectively. The height of each histogram bin indicates the percentage intensity contributing to the total R^{ea} for each structure. The bins are positioned according to n_{O} and n_{OH} values, with the color of each bin reflecting the average R^{ea} for that specific Al atom group. Figures (d), (e), and (f) present the full R^{ea} distribution at $T_{\text{E}} = 10$ K for the respective H/Al ratios (2, 1, and 0.2), corresponding again to ALD temperatures of 25°C, 50°C, and 120°C. These figures also highlight the R^{ea} values for significant Al ligand groups, illustrating their individual contributions to the overall distribution.

References

- [1] Vincenc Nemanič. Hydrogen permeation barriers: Basic requirements, materials selection, deposition methods, and quality evaluation. *Nucl. Mater. Energy*, 19:451–457, 2019.
- [2] Yufan Li, Francesco Barzagli, Peng Liu, Xiaohan Zhang, Zhao Yang, Min Xiao, Yangqiang Huang, Xiao Luo, Chao'en Li, He'an Luo, and Rui Zhang. Mechanism and Evaluation of Hydrogen Permeation Barriers: A Critical Review. *Ind. Eng. Chem. Res.*, 62(39):15752–15773, 2023.
- [3] Jan Plutnar and Martin Pumera. Applications of Atomic Layer Deposition in Design of Systems for Energy Conversion. *Small*, 17(39):2102088, 2021.
- [4] Sina Karimzadeh, Babak Safaei, Chris Yuan, and Tien-Chien Jen. Emerging Atomic Layer Deposition for the Development of High-Performance Lithium-Ion Batteries. *Electrochem. Energy Rev.*, 6(1):24, 2023.
- [5] Xiangbo Meng. Atomic and molecular layer deposition in pursuing better batteries. *J. Mater. Res.*, 36(1):2–25, 2021.
- [6] Ola Nilsen, Knut B Gandrud, Ruud Amund, and Fjellvåg Helmer. Atomic Layer Deposition for Thin-Film Lithium-Ion Batteries. In *At. Layer Depos. Energy Convers. Appl.*, pages 183–207. Wiley, 2017.
- [7] Carlos Guerra-Núñez, Hyung Gyu Park, and Ivo Utke. Atomic Layer Deposition for Surface and Interface Engineering in Nanostructured Photovoltaic Devices. In *At. Layer Depos. Energy Convers. Appl.*, pages 119–148. Wiley, 2017.
- [8] Bikesh Gupta, Md. Anower Hossain, Asim Riaz, Astha Sharma, Doudou Zhang, Hark Hoe Tan, Chennupati Jagadish, Kylie Catchpole, Bram Hoex, and Siva Karuturi. Recent Advances in Materials Design Using Atomic Layer Deposition for Energy Applications. *Adv. Funct. Mater.*, 32(3):2109105, 2022.
- [9] Zhi Xing, Junjun Xiao, Ting Hu, Xiangchuan Meng, Dengxue Li, Xiaotian Hu, and Yiwang Chen. Atomic Layer Deposition of Metal Oxides in Perovskite Solar Cells: Present and Future. *Small Methods*, 4(12):2000588, 2020.
- [10] Chengxu Shen, Zhigang Yin, Fionn Collins, and Nicola Pinna. Atomic Layer Deposition of Metal Oxides and Chalcogenides for High Performance Transistors. *Adv. Sci.*, 9(23):2104599, 2022.
- [11] Ae Rim Choi, Dong Hyun Lim, So-Yeon Shin, Hye Joo Kang, Dohee Kim, Ja-Yong Kim, Youngbae Ahn, Seung Wook Ryu, and Il-Kwon Oh. Review of Material Properties of Oxide Semiconductor Thin Films Grown by Atomic Layer Deposition for Next-Generation 3D Dynamic Random-Access Memory Devices. *Chem. Mater.*, 2024.
- [12] Brandon J O'Neill, David H K Jackson, Jechan Lee, Christian Canlas, Peter C Stair, Christopher L Marshall, Jeffrey W Elam, Thomas F Kuech, James A Dumesic, George W Huber, Brandon J O'Neill, David H K Jackson, Jechan Lee, Christian Canlas, Peter C Stair, Christopher L Marshall, Jeffrey W Elam, Thomas F Kuech, James A Dumesic, and George W Huber. Catalyst Design with Atomic Layer Deposition. *ACS Catal.*, 5(3):1804–1825, 2015.
- [13] Joseph A Singh, Nuoya Yang, and Stacey F Bent. Nanoengineering Heterogeneous Catalysts by Atomic Layer Deposition. *Annu. Rev. Chem. Biomol. Eng.*, 8(1):41–62, 2017.
- [14] Catherine Marichy and Nicola Pinna. Atomic Layer Deposition to Materials for Gas Sensing Applications. *Adv. Mater. Interfaces*, 3(21):1600335, 2016.
- [15] Octavio Graniel, Matthieu Weber, Sébastien Balme, Philippe Miele, and Mikhael Bechelany. Atomic layer deposition for biosensing applications. *Biosens. Bioelectron.*, 122:147–159, 2018.
- [16] Matthieu Weber, Anne Julbe, André Ayrat, Philippe Miele, and Mikhael Bechelany. Atomic Layer Deposition for Membranes: Basics, Challenges, and Opportunities. *Chem. Mater.*, 30(21):7368–7390, 2018.
- [17] Amir Hossein Behroozi, Vahid Vatanpour, Louise Meunier, Mohammad Mehrabi, and Ehssan H Koupaie. Membrane Fabrication and Modification by Atomic Layer Deposition: Processes and Applications in Water Treatment and Gas Separation. *ACS Appl. Mater. Interfaces*, 15(11):13825–13843, 2023.
- [18] Na Gong, Hangli Seet, Jing Cao, Tzee Luai Meng, Yong Wang, Dennis C C Tan, Chee Kiang Ivan Tan, Ady Suwardi, Qiang Zhu, Daniel J Blackwood, Mui Ling Sharon Nai, and Hongfei Liu. Atomic layer deposition of Al₂O₃ thin films for corrosion protections of additive manufactured and wrought stainless steels 316L. *Mater. Lett.*, 331:133434, 2023.

- [19] Lionel Santinacci. Atomic layer deposition: An efficient tool for corrosion protection. *Curr. Opin. Colloid Interface Sci.*, 63:101674, 2023.
- [20] Richard W Johnson, Adam Hultqvist, and Stacey F Bent. A brief review of atomic layer deposition: from fundamentals to applications. *Mater. Today*, 17(5):236–246, 2014.
- [21] Suja George, Prabhat Pandit, and A. B. Gupta. Residual aluminium in water defluoridated using activated alumina adsorption - Modeling and simulation studies. *Water Res.*, 44(10):3055–3064, 2010.
- [22] Christophe Detavernier, Jolien Dendooven, Sreeprasanth Pulinthanathu Sree, Karl F. Ludwig, and Johan A. Martens. Tailoring nanoporous materials by atomic layer deposition. *Chem. Soc. Rev.*, 40(11):5242–5253, 2011.
- [23] Thomas Keuter, Norbert Heribert Menzler, Georg Mauer, Frank Vondahlen, Robert Vaßen, and Hans Peter Buchkremer. Modeling precursor diffusion and reaction of atomic layer deposition in porous structures. *J. Vac. Sci. Technol. A Vacuum, Surfaces, Film.*, 33(1), 2015.
- [24] Jingming Zhang, Yicheng Li, Kun Cao, and Rong Chen. Advances in Atomic Layer Deposition. *Nanomanufacturing Metrol.*, 5(3):191–208, 2022.
- [25] Booyong S Lim, Antti Rahtu, and Roy G Gordon. Atomic layer deposition of transition metals. *Nat. Mater.*, 2(11):749–754, 2003.
- [26] Kwanpyo Kim, Han-Bo-Ram Lee, Richard W Johnson, Jukka T Tanskanen, Nan Liu, Myung-Gil Kim, Changhyun Pang, Chiyui Ahn, Stacey F Bent, and Zhenan Bao. Selective metal deposition at graphene line defects by atomic layer deposition. *Nat. Commun.*, 5(1):4781, 2014.
- [27] Mikko Ritala, Kaupo Kukli, Antti Rahtu, Petri I Räisänen, Markku Leskelä, Timo Sajavaara, and Juhani Keinonen. Atomic Layer Deposition of Oxide Thin Films with Metal Alkoxides as Oxygen Sources. *Science (80-.)*, 288(5464):319–321, 2000.
- [28] Joice Sophia Ponraj, Giovanni Attolini, and Matteo Bosi. Review on Atomic Layer Deposition and Applications of Oxide Thin Films. *Crit. Rev. Solid State Mater. Sci.*, 38(3):203–233, 2013.
- [29] Bart Macco and W M M (Erwin) Kessels. Atomic layer deposition of conductive and semiconductive oxides. *Appl. Phys. Rev.*, 9(4):41313, 2022.
- [30] Henrik Hovde Sønsteby, Helmer Fjellvåg, and Ola Nilsen. Functional Perovskites by Atomic Layer Deposition – An Overview. *Adv. Mater. Interfaces*, 4(8):1600903, 2017.
- [31] Adriaan J M Mackus, Joel R Schneider, Callisto MacIsaac, Jon G Baker, and Stacey F Bent. Synthesis of Doped, Ternary, and Quaternary Materials by Atomic Layer Deposition: A Review. *Chem. Mater.*, 31(4):1142–1183, 2019.
- [32] W Hao, C Marichy, and C Journet. Atomic layer deposition of stable 2D materials. *2D Mater.*, 6(1):12001, 2018.
- [33] Carlos Guerra-Nuñez, Max Döbeli, Johann Michler, and Ivo Utke. Reaction and Growth Mechanisms in Al₂O₃ deposited via Atomic Layer Deposition: Elucidating the Hydrogen Source. *Chem. Mater.*, 29(20):8690–8703, 2017.
- [34] Claudia Cancellieri, Simon Gramatte, Olivier Politano, Léo Lapeyre, Fedor F. Klimashin, Krzysztof Mackosz, Ivo Utke, Zbynek Novotny, Arnold M. Müller, Christof Vockenhuber, Vladyslav Turlo, and Lars P.H. H Jeurgens. Effect of hydrogen on the chemical state, stoichiometry and density of amorphous Al₂O₃ films grown by thermal atomic layer deposition. *Surf. Interface Anal.*, 56(5):293–304, 2024.
- [35] Mikko Ruoho, Janne-Petteri Niemelä, Carlos Guerra-Nunez, Natalia Tarasiuk, Georgina Robertson, Aidan A Taylor, Xavier Maeder, Czeslaw Kapusta, Johann Michler, and Ivo Utke. Thin-Film Engineering of Mechanical Fragmentation Properties of Atomic-Layer-Deposited Metal Oxide. *Nanomaterials*, 10(3):558, 2020.
- [36] Jochen M. Schneider, Karin Larsson, Jun Lu, Eva Olsson, and Björgvin Hjörvarsson. Role of hydrogen for the elastic properties of alumina thin films. *Appl. Phys. Lett.*, 80(7):1144–1146, 2002.
- [37] Suyeon Kim, Seung-Hun Lee, In Ho Jo, Jongsu Seo, Yeong-Eun Yoo, and Jeong Hwan Kim. Influence of growth temperature on dielectric strength of Al₂O₃ thin films prepared via atomic layer deposition at low temperature. *Sci. Rep.*, 12(1):5124, 2022.
- [38] Caroline S Gorham, John T Gaskins, Gregory N Parsons, Mark D Losego, and Patrick E Hopkins. Density dependence of the room temperature thermal conductivity of atomic layer deposition-grown amorphous alumina (Al₂O₃). *Appl. Phys. Lett.*, 104(25):253107, 2014.
- [39] L. Jeurgens, W. Sloof, F. Tichelaar, and E. Mittemeijer. Thermodynamic stability of amorphous oxide films on metals: Application to aluminum oxide films on aluminum substrates. *Phys. Rev. B - Condens. Matter Mater. Phys.*, 62(7):4707–4719, 2000.

- [40] P. C. Snijders, L. P.H. H Jeurgens, and W. G. Sloof. Structural ordering of ultra-thin, amorphous aluminium-oxide films. *Surf. Sci.*, 589(1-3):98–105, 2005.
- [41] J. P. Holgado, A. Caballero, J. P. Espinós, J. Morales, V. M. Jiménez, A. Justo, and A. R. González-Elipe. Characterization by X-ray absorption spectroscopy of oxide thin films prepared by ion beam-induced CVD. *Thin Solid Films*, 377-378:460–466, 2000.
- [42] Sung Bo Keun Lee, Sung Bo Keun Lee, Sun Young Park, Yoo Soo Yi, and Chi Won Ahn. Structure of amorphous aluminum oxide. *Phys. Rev. Lett.*, 103(9):4–7, 2009.
- [43] Simon Gramatte, Lars P. H. Jeurgens, Olivier Politano, Jose Antonio Simon Greminger, Florence Baras, Angelos Xomalis, and Vladyslav Turlo. Atomistic Simulations of the Crystalline-to-Amorphous Transformation of γ -Al₂O₃ Nanoparticles: Delicate Interplay between Lattice Distortions, Stresses, and Space Charges. *Langmuir*, 39(18):6301–6315, may 2023.
- [44] Nina S. Genz, Antti Jussi Kallio, Florian Meirer, Simo Huotari, and Bert M. Weckhuysen. Operando Laboratory-based X-ray Absorption Spectroscopy: Guidelines for Newcomers in the Field. *Chemistry Methods*, 4(1), 2024.
- [45] John F. Watts and James E. Castle. The development of laboratory-based high energy sources for XPS. *Surf. Interface Anal.*, 56(7):408–424, 2024.
- [46] Lars P.H. H Jeurgens, Claudia Cancellieri, Andreas Borgschulte, and John F. Watts. Advancements and challenges of HAXPES for materials sciences and technologies. *Surf. Interface Anal.*, 56(7):397–398, jul 2024.
- [47] C. D. Wagner. Chemical shifts of Auger lines, and the Auger parameter. *Faraday Discuss. Chem. Soc.*, 60:291–300, 1975.
- [48] C.D. D. Wagner and A. Joshi. The auger parameter, its utility and advantages: a review. *J. Electron Spectros. Relat. Phenom.*, 47(C):283–313, 1988.
- [49] Giuliano Moretti. Auger parameter and Wagner plot in the characterization of chemical states by X-ray photoelectron spectroscopy: A review. *J. Electron Spectros. Relat. Phenomena*, 95(2-3):95–144, 1998.
- [50] L.P.H. Jeurgens, W.G. Sloof, F.D. Tichelaar, and E.J. Mittemeijer. Composition and chemical state of the ions of aluminium-oxide films formed by thermal oxidation of aluminium. *Surf. Sci.*, 506(3):313–332, 2002.
- [51] C D Wagner, D E Passoja, H F Hillery, T G Kinisky, H A Six, W T Jansen, and J A Taylor. Auger and photoelectron line energy relationships in aluminum–oxygen and silicon–oxygen compounds. *J. Vac. Sci. Technol.*, 21(4):933–944, 1982.
- [52] Yoshikazu KAMESHIMA, Atsuo YASUMORI, and Kiyoshi OKADA. XPS and X-ray AES (XAES) Study of Various Aluminate Compounds. *Hyomen Kagaku*, 21(8):481–487, 2000.
- [53] C. J. Powell. Recommended Auger parameters for 42 elemental solids. *J. Electron Spectros. Relat. Phenom.*, 185(1-2):1–3, 2012.
- [54] Francesco Ambrosio, Alfredo Pasquarello, Olga Guseva, Raheleh Partovi Nia, Roland Hauert, Erwin Hack, Lars P.H. H H Jeurgens, Patrik Schmutz, and Claudia Cancellieri. Electronic and structural characterization of barrier-type amorphous aluminium oxide. *Electrochim. Acta*, 224:503–516, 2017.
- [55] James E. Castle. A unified scale for the Auger parameter: Methodology and benefits. *Surf. Interface Anal.*, 54(4):455–464, 2022.
- [56] Giuliano Moretti. The use of the oxygen Auger parameters in the characterisation of oxygen-containing compounds. *J. Electron Spectros. Relat. Phenomena*, 58(1-2):105–118, mar 1992.
- [57] J A D Matthew and S Parker. Correlations between the Auger parameters of oxygen and metal atoms in oxygen-containing compounds. *J. Electron Spectros. Relat. Phenomena*, 85(1):175–178, 1997.
- [58] L P H Jeurgens, F Reichel, S Frank, G Richter, and E J Mittemeijer. On the development of long-range order in ultra-thin amorphous Al₂O₃ films upon their transformation into crystalline gamma-Al₂O₃. *Surf. Interface Anal.*, 40(3-4):259–263, 2008.
- [59] Georgijs Bakradze, Lars P H Jeurgens, and Eric J Mittemeijer. Valence-Band and Chemical-State Analyses of Zr and O in Thermally Grown Thin Zirconium-Oxide Films: An XPS Study. *J. Phys. Chem. C*, 115(40):19841–19848, oct 2011.
- [60] V.R Palkar, D Thapa, M.S Multani, and S.G Malghan. Densification of nanostructured alumina assisted by rapid nucleation of α -alumina. *Mater. Lett.*, 36(5-6):235–239, 1998.
- [61] F Zigan, W Joswig, and N Burger. Die Wasserstoffpositionen im Bayerit, Al(OH)₃. *Zeitschrift für Krist. - Cryst. Mater.*, 148(3-4):255–274, 1978.

- [62] Francesco Filippone and Giuliano Moretti. Oxide electronic polarizabilities and aluminum coordination at the outer surface of zeolites obtained by X-ray photoelectron spectroscopy. *Appl. Surf. Sci.*, 135(1-4):150–162, 1998.
- [63] Sebastian Siol, Jennifer Mann, John Newman, Takuya Miyayama, Katsumi Watanabe, Patrik Schmutz, Claudia Cancellieri, and Lars P.H. H Jeurgens. Concepts for chemical state analysis at constant probing depth by lab-based XPS/HAXPES combining soft and hard X-ray sources. *Surf. Interface Anal.*, 52(12):802–810, 2020.
- [64] Aidan P. Thompson, H. Metin Aktulga, Richard Berger, Dan S. Bolintineanu, W. Michael Brown, Paul S. Crozier, Pieter J. in 't Veld, Axel Kohlmeyer, Stan G. Moore, Trung Dac Nguyen, Ray Shan, Mark J. Stevens, Julien Tranchida, Christian Trott, and Steven J. Plimpton. LAMMPS - a flexible simulation tool for particle-based materials modeling at the atomic, meso, and continuum scales. *Comput. Phys. Commun.*, 271:108171, 2022.
- [65] Dilipkumar N. Asthagiri and Thomas L. Beck. MD Simulation of Water Using a Rigid Body Description Requires a Small Time Step to Ensure Equipartition. *J. Chem. Theory Comput.*, 20(1):368–374, 2024.
- [66] Anubhav Jain, Geoffroy Hautier, Charles J. Moore, Shyue Ping Ong, Christopher C. Fischer, Tim Mueller, Kristin A. Persson, and Gerbrand Ceder. A high-throughput infrastructure for density functional theory calculations. *Comput. Mater. Sci.*, 50(8):2295–2310, 2011.
- [67] A H Larsen. The Atomic Simulation Environment - A Python library for working with atoms. *J. Phys. Condens. Matter*, 29:273002, 2012.
- [68] Alexander Stukowski. Visualization and analysis of atomistic simulation data with OVITO-the Open Visualization Tool. *Model. Simul. Mater. Sci. Eng.*, 18(1):1–7, 2010.
- [69] So Takamoto, Chikashi Shinagawa, Daisuke Motoki, Kosuke Nakago, Wenwen Li, Iori Kurata, Taku Watanabe, Yoshihiro Yayama, Hiroki Iriguchi, Yusuke Asano, Tasuku Onodera, Takafumi Ishii, Takao Kudo, Hideki Ono, Ryohto Sawada, Ryuichiro Ishitani, Marc Ong, Taiki Yamaguchi, Toshiki Kataoka, Akihide Hayashi, Nontawat Charoenphakdee, and Takeshi Ibuka. Towards universal neural network potential for material discovery applicable to arbitrary combination of 45 elements. *Nat. Commun.*, 13(1):2991, 2022.
- [70] Simon Gramatte, Vladyslav Turlo, and Olivier Politano. Do we really need machine learning interatomic potentials for modeling amorphous metal oxides? Case study on amorphous alumina by recycling an existing ab initio database. *Model. Simul. Mater. Sci. Eng.*, 32(4):45010, 2024.
- [71] So Takamoto, Chikashi Shinagawa, Daisuke Motoki, Kosuke Nakago, Wenwen Li, Iori Kurata, Taku Watanabe, Yoshihiro Yayama, Hiroki Iriguchi, Yusuke Asano, Tasuku Onodera, Takafumi Ishii, Takao Kudo, Hideki Ono, Ryohto Sawada, Ryuichiro Ishitani, Marc Ong, Taiki Yamaguchi, Toshiki Kataoka, Akihide Hayashi, Nontawat Charoenphakdee, and Takeshi Ibuka. Matlantis, software as a service style material discovery tool.
- [72] F. Reichel, L. P.H. H H Jeurgens, G. Richter, and E. J. Mittemeijer. Amorphous versus crystalline state for ultrathin Al₂O₃ overgrowths on Al substrates. *J. Appl. Phys.*, 103(9), 2008.
- [73] Jinliu Wang, Yuan Hsin Yu, S. C. Lee, and Yip Wah Chung. Tribological and optical properties of crystalline and amorphous alumina thin films grown by low-temperature reactive magnetron sputter-deposition. *Surf. Coatings Technol.*, 146-147:189–194, 2001.
- [74] G. Angarita, C. Palacio, M. Trujillo, and M. Arroyave. Synthesis of Alumina Thin Films Using Reactive Magnetron Sputtering Method. *J. Phys. Conf. Ser.*, 850(1):0–4, 2017.
- [75] J. K. Christie. Review: Understanding the properties of amorphous materials with high-performance computing methods. *Philos. Trans. R. Soc. A Math. Phys. Eng. Sci.*, 381(2250), 2023.
- [76] Jack Strand and Alexander L. Shluger. On the Structure of Oxygen Deficient Amorphous Oxide Films. *Adv. Sci.*, 2306243:1–14, 2023.
- [77] Aditya Sundar, Jianguo Yu, Liang Qi, and M. Nedim Cinbiz. High temperature stability and transport characteristics of hydrogen in alumina via multiscale computation. *Int. J. Hydrogen Energy*, 47(75):32345–32357, 2022.
- [78] Simon Gramatte, Olivier Politano, Claudia Cancellieri, Ivo Utke, Lars P. H. Jeurgens, and Vladyslav Turlo. Effect of hydrogen on the local chemical bonding states and structure of amorphous alumina by atomistic and electrostatic modeling of auger parameter shifts, 2024.
- [79] R. Dupree, I. Farnan, A. J. Forty, S. El-Mashri, and L. Bottyan. A MAS NMR STUDY OF THE STRUCTURE OF AMORPHOUS ALUMINA FILMS. *Le J. Phys. Colloq.*, 46(C8):C8–113–C8–117, dec 1985.

- [80] Brent T Poe, Paul F. McMillan, Bertrand Cote, Dominique Massiot, and Jean Pierre Coutures. Silica-alumina liquids: in-situ study by high-temperature aluminum-27 NMR spectroscopy and molecular dynamics simulation. *J. Phys. Chem.*, 96(21):8220–8224, oct 1992.
- [81] Stuart Ansell, Shankar Krishnan, J K Richard Weber, John J Felten, Paul C Nordine, Mark A Beno, David L Price, and Marie-louise Saboungi. Structure of Liquid Aluminum Oxide. *Phys. Rev. Lett.*, 78(3):464–466, jan 1997.
- [82] Jinlei Cui, Matthew G. Kast, Blake A. Hammann, Yvonne Afriyie, Keenan N. Woods, Paul N. Plassmeyer, Cory K. Perkins, Zayd L. Ma, Douglas A. Keszler, Catherine J. Page, Shannon W. Boettcher, and Sophia E. Hayes. Aluminum Oxide Thin Films from Aqueous Solutions: Insights from Solid-State NMR and Dielectric Response. *Chem. Mater.*, 30(21):7456–7463, 2018.
- [83] Gonzalo Gutiérrez, A B Belonoshko, Rajeev Ahuja, and Börje Johansson. Structural properties of liquid Al₂O₃ A molecular dynamics study. *Phys. Rev. E - Stat. Physics, Plasmas, Fluids, Relat. Interdiscip. Top.*, 61(3):2723–2729, 2000.
- [84] C. Landron, L. Hennet, T. E. Jenkins, G. N. Greaves, J. P. Coutures, and A. K. Soper. Liquid alumina: Detailed atomic coordination determined from neutron diffraction data using empirical potential structure refinement. *Phys. Rev. Lett.*, 86(21):4839–4842, 2001.
- [85] Karl Wefers and Chanakya Misra. Oxides and Hydroxides of Aluminum. *Alcoa Tech. Pap.*, 19:1–100, 1987.
- [86] Shigemi Kohiki, Shinji Ozaki, Tomoko Hamada, and Kazuo Taniguchi. Characterization of silicon compounds using the Auger parameter in X-ray Photoelectron Spectroscopy (XPS). *Appl. Surf. Sci.*, 28(2):103–110, 1987.
- [87] M. J. Edgell, R. W. Paynter, S. C. Mugford, and J. E. Castle. An XPS study of cation-exchanged Y-type zeolites. *Zeolites*, 10(1):51–60, 1990.
- [88] L. Fiermans, R. Hoogewijs, and J. Vennik. Electron spectroscopy of transition metal oxide surfaces. *Surf. Sci.*, 47(1):1–40, 1975.
- [89] G. Moretti. The Auger parameter and the polarization energy: A simple electrostatic model. *Surf. Interface Anal.*, 16(1-12):159–162, 1990.
- [90] Giuliano Moretti. Auger parameter shifts in the case of the non-local screening mechanism: Applications of the electrostatic model to molecules, solids and adsorbed species. *Surf. Interface Anal.*, 17(6):352–356, 1991.
- [91] Matthias Seeger. Gaussian Processes for Machine Learning University of California at Berkeley. *Int. J. Neural Syst.*, 14:69–109, 2004.
- [92] Eric Brochu, Vlad M. Cora, and Nando de Freitas. A Tutorial on Bayesian Optimization of Expensive Cost Functions, with Application to Active User Modeling and Hierarchical Reinforcement Learning. *arXiv*, dec 2010.
- [93] Carl Edward Rasmussen and Christopher K. I. Williams. *Gaussian Processes for Machine Learning*. The MIT Press, 2005.
- [94] Fernando Nogueira, The Materials Project, M Huttula, L Partanen, A Mäkinen, T Kantia, H Aksela, S Aksela, J A D Matthew, S Parker, Lars P H Jeurgens, F Reichel, S Frank, G Richter, Eric J Mittemeijer, R DUPREE, I FARNAN, A J FORTY, S ELMASHRI, L BOTTYAN, Georgijs Bakradze, Lars P H Jeurgens, Eric J Mittemeijer, P C Snijders, Lars P H Jeurgens, W G Sloof, F Zigan, W Joswig, N Burger, Zhendong Guo, Francesco Ambrosio, Alfredo Pasquarello, Aditya Sundar, Jianguo Yu, Liang Qi, and M. Nedim Cimbiz. Valence-Band and Chemical-State Analyses of Zr and O in Thermally Grown Thin Zirconium-Oxide Films: An XPS Study. *Surf. Interface Anal.*, 496(3-4):175–178, feb 1985.
- [95] Jack R. Tessman, A. H. Kahn, and William Shockley. Electronic Polarizabilities of Ions in Crystals. *Phys. Rev.*, 92(4):890–895, nov 1953.
- [96] G. Kresse and J. Hafner. Ab initio molecular dynamics for liquid metals. *Phys. Rev. B*, 47(1):558–561, 1993.
- [97] G. Kresse and J. Hafner. Ab initio molecular-dynamics simulation of the liquid-metalamorphous-semiconductor transition in germanium. *Phys. Rev. B*, 49(20):14251–14269, 1994.
- [98] G. Kresse and J. Furthmüller. Efficient iterative schemes for ab initio total-energy calculations using a plane-wave basis set. *Phys. Rev. B*, 54(16):11169–11186, oct 1996.
- [99] G. Kresse and J. Furthmüller. Efficiency of ab-initio total energy calculations for metals and semiconductors using a plane-wave basis set. *Comput. Mater. Sci.*, 6(1):15–50, 1996.

- [100] P. E. Blöchl. Projector augmented-wave method. *Phys. Rev. B*, 50(24):17953–17979, 1994.
- [101] D. Joubert. From ultrasoft pseudopotentials to the projector augmented-wave method. *Phys. Rev. B - Condens. Matter Mater. Phys.*, 59(3):1758–1775, 1999.
- [102] John P. Perdew, Kieron Burke, and Matthias Ernzerhof. Generalized gradient approximation made simple. *Phys. Rev. Lett.*, 77(18):3865–3868, 1996.
- [103] J. P. Perdew and Alex Zunger. Self-interaction correction to density-functional approximations for many-electron systems. *Phys. Rev. B*, 23(10):5048–5079, may 1981.
- [104] Stefan Grimme, Jens Antony, Stephan Ehrlich, and Helge Krieg. A consistent and accurate ab initio parametrization of density functional dispersion correction (DFT-D) for the 94 elements H-Pu. *J. Chem. Phys.*, 132(15), 2010.
- [105] Graeme Henkelman, Andri Arnaldsson, and Hannes Jónsson. A fast and robust algorithm for Bader decomposition of charge density. *Comput. Mater. Sci.*, 36(3):354–360, 2006.
- [106] Min Yu and Dallas R. Trinkle. Accurate and efficient algorithm for Bader charge integration. *J. Chem. Phys.*, 134(6), 2011.
- [107] Edward Sanville, Steven D. Kenny, Roger Smith, and Graeme Henkelman. Improved grid-based algorithm for Bader charge allocation. *J. Comput. Chem.*, 28(5):899–908, apr 2007.
- [108] W. Tang, E. Sanville, and G. Henkelman. A grid-based Bader analysis algorithm without lattice bias. *J. Phys. Condens. Matter*, 21(8), 2009.
- [109] Giuliano Moretti and Horst P. Beck. Relationship between the Auger parameter and the ground state valence charge at the core-ionized site. *Surf. Interface Anal.*, 52(12):864–868, 2020.
- [110] Horst P. Beck and Giuliano Moretti. Physical genetics: Cross-breeding density functional theory and X-ray photoelectron spectroscopy to rationalize chemical shifts of binding energies in solid compounds. *Solid State Sci.*, 110(July):106359, 2020.
- [111] Simon Gramatte, Lars P. H. Jeurgens, Olivier Politano, Jose Antonio Simon Greminger, Florence Baras, Angelos Xomalis, Vladyslav Turlo, Jose Antonio Simon Greminger, Florence Baras, Angelos Xomalis, Vladyslav Turlo, Jose Antonio Simon Greminger, Florence Baras, Angelos Xomalis, and Vladyslav Turlo. Atomistic simulations of the crystalline-to-amorphous transformation of gamma-Al₂O₃ nanoparticles: delicate interplay between lattice distortions, stresses, and space charges. *Langmuir*, 39(18):6301–6315, may 2022.
- [112] P C Snijders, L P H Jeurgens, and W G Sloof. Structure of thin aluminium-oxide films determined from valence band spectra measured using XPS. *Surf. Sci.*, 496(1):97–109, 2002.
- [113] Goro Yamaguchi, Itaru Yasui, and Wen-Chau Chiu. A New Method of Preparing Theta-Alumina and the Interpretation of Its X-Ray-powder Diffraction Pattern and Electron Diffraction Pattern. *Bull. Chem. Soc. Jpn.*, 43(8):2487–2491, 1970.
- [114] Matthias J Young, Nicholas M Bedford, Angel Yanguas-Gil, Steven Letourneau, Matthew Coile, David J Mandia, Bachir Aoun, Andrew S Cavanagh, Steven M George, and Jeffrey W. Elam. Probing the Atomic-Scale Structure of Amorphous Aluminum Oxide Grown by Atomic Layer Deposition. *ACS Appl. Mater. Interfaces*, 12(20):22804–22814, 2020.
- [115] Zhendong Guo, Francesco Ambrosio, and Alfredo Pasquarello. Extrinsic Defects in Amorphous Oxides: Hydrogen, Carbon, and Nitrogen Impurities in Alumina. *Phys. Rev. Appl.*, 11(2):1, 2019.
- [116] A. B. Belonoshko, A. Rosengren, Q. Dong, G. Hultquist, and C. Leygraf. First-principles study of hydrogen diffusion in alpha - Al₂O₃ and liquid alumina. *Phys. Rev. B - Condens. Matter Mater. Phys.*, 69(2):1–6, 2004.
- [117] Robert D. Shannon and Reinhard X. Fischer. Empirical electronic polarizabilities in oxides, hydroxides, oxyfluorides, and oxychlorides. *Phys. Rev. B - Condens. Matter Mater. Phys.*, 73(23):1–28, 2006.
- [118] Heleen van Gog. First-principles study of dehydration interfaces between diaspore and corundum, gibbsite and boehmite, and boehmite and γ -Al₂O₃: Energetic stability, interface charge effects, and dehydration defects. *Appl. Surf. Sci.*, 541(November 2020), 2021.
- [119] Larry W. Finger and Robert M. Hazen. Crystal structure and compression of ruby to 46 kbar. *J. Appl. Phys.*, 49(12):5823–5826, 1978.
- [120] R. H. Meinhold, R. C.T. T Slade, and R. H. Newman. High field MAS NMR, with simulations of the effects of disorder on lineshape, applied to thermal transformations of alumina hydrates. *Appl. Magn. Reson.*, 4(1-2):121–140, 1993.

- [121] G. Kunath-Fandrei, T. J. Bastow, J. S. Hall, C. Jäger, and M. E. Smith. Quantification of aluminum coordinations in amorphous aluminas by combined central and satellite transition magic angle spinning NMR spectroscopy. *J. Phys. Chem.*, 99(41):15138–15141, 1995.
- [122] K.J.D. J D MacKenzie, J. Temuujin, and K. Okada. Thermal decomposition of mechanically activated sphalerite. *Thermochim. Acta*, 180(C):117–123, apr 1991.
- [123] Daniel Lee, Nghia Tuan Duong, Olivier Lafon, and Gaël De Paëpe. Primostrato solid-state NMR enhanced by dynamic nuclear polarization: Pentacoordinated Al³⁺ ions are only located at the surface of hydrated gamma-alumina. *J. Phys. Chem. C*, 118(43):25065–25076, 2014.
- [124] Caijuan Shi, Oliver L.G. G Alderman, Diana Berman, Jincheng Du, Joerg Neuefeind, Anthony Tamalonis, J. K.Richard Weber, Jinglin You, and Chris J. Benmore. The structure of amorphous and deeply supercooled liquid alumina. *Front. Mater.*, 6(March):1–15, 2019.
- [125] Sergio Davis and Gonzalo Gutiérrez. Structural, elastic, vibrational and electronic properties of amorphous Al₂O₃ from ab initio calculations. *J. Phys. Condens. Matter*, 23(49), 2011.
- [126] Suochang Xu, Nicholas R. Jaegers, Wenda Hu, Ja Hun Kwak, Xinhe Bao, Junming Sun, Yong Wang, and Jian Zhi Hu. High-Field One-Dimensional and Two-Dimensional ²⁷Al Magic-Angle Spinning Nuclear Magnetic Resonance Study of theta-, delta-, and gamma-Al₂O₃ Dominated Aluminum Oxides: Toward Understanding the Al Sites in gamma-Al₂O₃. *ACS Omega*, 6(5):4090–4099, 2021.
- [127] David J. Morgan. XPS insights: Asymmetric peak shapes in XPS. *Surf. Interface Anal.*, 55(8):567–571, 2023.
- [128] Dinh Loc Duong, Seok Joon Yun, and Young Hee Lee. Van der Waals Layered Materials: Opportunities and Challenges. *ACS Nano*, 11(12):11803–11830, 2017.
- [129] Ariel Lozano, Bruno Escribano, Elena Akhmatskaya, and Javier Carrasco. Assessment of van der Waals inclusive density functional theory methods for layered electroactive materials. *Phys. Chem. Chem. Phys.*, 19(15):10133–10139, 2017.
- [130] Jonas Moellmann and Stefan Grimme. DFT-D3 study of some molecular crystals. *J. Phys. Chem. C*, 118(14):7615–7621, 2014.
- [131] Gabriella Graziano, Jií Klimeš, Felix Fernandez-Alonso, and Angelos Michaelides. Improved description of soft layered materials with van der Waals density functional theory. *J. Phys. Condens. Matter*, 24(42), 2012.
- [132] Stefan Grimme, Stephan Ehrlich, and Lars Goerigk. Effect of the damping function in dispersion corrected density functional theory. *J. Comput. Chem.*, 32(7):1456–1465, may 2011.
- [133] Jan Hermann, Robert A. DiStasio, and Alexandre Tkatchenko. First-Principles Models for van der Waals Interactions in Molecules and Materials: Concepts, Theory, and Applications. *Chem. Rev.*, 117(6):4714–4758, 2017.
- [134] Pfneth-research. torch-dftd, 2023.
- [135] Julian D. Gale, Andrew L. Rohl, Victor Milman, and Michele C. Warren. An ab initio study of the structure and properties of aluminum hydroxide: Gibbsite and bayerite. *J. Phys. Chem. B*, 105(42):10236–10242, 2001.
- [136] The Materials Project. Materials Data on Al₂O₃ by Materials Project. *Mater. Proj.*, 2020.
- [137] C. Landron, A. K. Soper, T. E. Jenkins, G. N. Greaves, L. Hennet, and J. P. Coutures. Measuring neutron scattering structure factor for liquid alumina and analysing the radial distribution function by empirical potential structural refinement. *J. Non. Cryst. Solids*, 293-295(1):453–457, 2001.
- [138] Pierre Florian, Dominique Massiot, Brent Poe, Ian Farnan, and Jean Pierre Coutures. A time resolved ²⁷Al NMR study of the cooling process of liquid alumina from 2450 °C to crystallisation. *Solid State Nucl. Magn. Reson.*, 5(3):233–238, 1995.